Delft University of Technology

Development and experimental evaluation of surface enhancement methods for laser powder directed energy deposition microchannels

Gradl, P.R.; Cervone, A.; Colonna, Piero

**Citation (APA)**
Gradl, P. R., Cervone, A., & Colonna, P. (2024). Development and experimental evaluation of surface enhancement methods for laser powder directed energy deposition microchannels. *Virtual and Physical Prototyping*, *19*(1), Article e2345389. https://doi.org/10.1080/17452759.2024.2345389
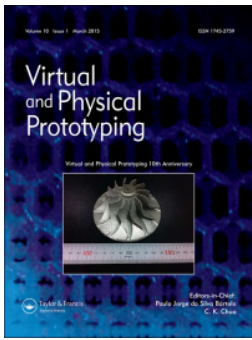
**Important note**
To cite this publication, please use the final published version (if applicable).
Please check the document version above.

# Development and experimental evaluation of surface enhancement methods for laser powder directed energy deposition microchannels

## Paul Gradl, Angelo Cervone & Piero Colonna

View supplementary material ⬀

Published online: 08 May 2024.

Submit your article to this journal ⬀

Article views: 51

View related articles ⬀

View Crossmark data ⬀

Taylor & Francis
Taylor & Francis Group

# Development and experimental evaluation of surface enhancement methods for laser powder directed energy deposition microchannels

Paul Gradl [a], Angelo Cervone [b] and Piero Colonna [c]

aPropulsion Department, NASA Marshall Space Flight Center, Huntsville, AL, USA; bSpace Systems Engineering, Delft University of Technology, Delft, Netherlands; cPropulsion and Power, Delft University of Technology, Delft, Netherlands

**ABSTRACT**

This research evaluates Laser Powder Directed Energy Deposition (LP-DED) for producing fine feature internal microchannels. This study is focused on enhancing and characterising the surfaces of microchannels produced using techniques such as abrasive flow machining, chemical milling, chemical mechanical polishing, electrochemical machining, and thermal energy method to modify internal surfaces of microchannels made from NASA HR-1 Fe-Ni-Cr alloy. Flow testing for discharge coefficient measurement is conducted on processed microchannel samples, followed by characterisation through optical microscopy, Scanning Electron Microscopy (SEM), and Computed Tomography. Findings reveal variations in surfaces due to powder adherence, melt pool undulations, and polishing mechanisms. The study emphasises the significance of removing material equivalent to the mean powder diameter to reduce surface roughness and impact the discharge coefficient. The research proposes a ratio for planarising roughness and waviness peak height and density, offering insights for tailored surface adjustments in specific applications requiring reduced flow resistance.

## Highlights

- Internal microchannels with thin-walls were fabricated using the laser powder directed energy deposition process.
- Various surface enhancements and polishing processes were developed to modify the surface texture of the LP-DED channels.
- Flow testing was conducted to determine the discharge coefficient.
- Post-test characterisation was completed to obtain cross sectional area, perimeter, surface texture, and general surface condition to analyse results.
- Ratio of roughness and waviness peak and density (Spk/Spd and Wp/WPc) is proposed as a relevant surface characterisation parameter.
- Tailored surface modifications for specific end-use applications.

## Terminology

| | |
|---|---|
| AFM | Abrasive flow machining |
| AM | Additive manufacturing |
| Cd | Discharge coefficient |
| CM | Chemical milling |
| CMP | Chemical mechanical polishing |
| DED | directed energy deposition |
| DfAM | Design for additive manufacturing |
| F | powder feedrate, in grams/min |
| λc | large-scale band pass filter (also Lc) |
| λs | small-scale (noise) filter (also Ls) |
| L-PBF | Laser powder bed fusion |
| LP-DED | laser powder directed energy deposition |
| NASA HR-1 | Fe-Ni-Cr alloy for hydrogen resistant applications |
| P | Power, in watts |
| PBF | powder bed fusion |
| PECM | Pulsed electrochemical machining |
| PSD | particle size distribution |
| Ra | Arithmetic mean directional roughness |
| Rz | Average directional maximum profile height |
| Sa | Average texture |
| SEM | Scanning Electron Microscope |
| Sk | Core texture depth |
| Spd | Roughness Peak Density |
| Spk | Reduced peak height |
| Sz | Maximum surface height |
| TEM | Thermal energy method |
| V | Traverse scan speed of deposition head, in mm/min |
| Wa | Arithmetic mean directional waviness |
| Wp | Waviness peak height |
| WPc | Waviness peak density |

## 1. Introduction

Metal additive manufacturing (AM) is being established as a manufacturing solution across various industries

and has rapidly grown from a prototyping tool to production of parts and systems. AM provides substantial benefits in terms of decreased processing time and cost, along with several technical advantages. These advantages encompass the potential to attain increased hardware complexity aimed at improved performance, the consolidation of parts, and the ability to process novel alloys. Various metal AM processes are being matured and require careful selection based on specific component requirements. These requirements encompass diverse build sizes, microstructures, and properties due to different melting or solid-state bonding techniques, and a wide spectrum of geometries, spanning from coarse to finely detailed features. These high-level process categories include powder bed fusion (PBF), directed energy deposition (DED), and solid-state techniques (cold spray, ultrasonic additive manufacturing, additive friction stir deposition, and binder jetting) [1]. These metal AM processes are being developed and actively used in aerospace, energy, automotive, medical, and industrial applications [2,3].

Metal AM is increasingly being used for the manufacturing of heat exchangers, particularly those featuring intricate internal channels that are thin-walled and carry pressurised fluids, such as cryogenic or high-temperature propellants [4]. Heat exchangers are utilised in a diverse array of components and systems, including combustion chambers in gas turbines and internal combustion engines, air supply and thermal management in fuel cells, industrial moulds and tooling, thermal management in electric batteries, evaporators and recuperators within waste-heat-to-power systems, as well as rocket engines [4–6]. These heat exchangers must meet a myriad of design requirements such as efficient heat transfer, minimal pressure losses, compact packaging, low weight, extended service life, and programmatic considerations.

Laser powder bed fusion (L-PBF) is currently the most common metal AM process and it is researched for various applications for aerospace and aviation, industrial, and medical [7–10]. Common applications using L-PBF focus on fine feature complex components such as include heat exchangers, combustion chambers, injectors, valves, hydraulic components, turbines, and turbomachinery [1,11–13]. L-PBF enables the production of intricate features with high complexity, including thin walls and internal features measuring 0.25 mm or smaller [14–16]. Researchers have focused on the interactions of L-PBF process parameters [17–19], geometric complexity [20–22], material and feedstock [6,23], and pressure and thermal performance of heat exchanger microchannels [24–26]. While L-PBF is common for components such as heat exchangers, its potential is restricted when it comes to achieving overall build volumes with diameters larger than 600 mm and height taller than 1 metre [1]. For parts that are beyond this size, laser powder directed energy deposition (LP-DED) is a viable alternative for integral microchannel heat exchangers, but very limited research has been conducted on thin-walled microchannels manufactured using this process [27,28]. LP-DED has traditionally been used as a process to produce simple near net shapes (i.e. forgings and castings), cladding and coating of surfaces, enhancements to components, and repair of parts [29,30]. The LP-DED process is rapidly maturing as a process to produce components with fine internal features, such as integral channels [5,31].

LP-DED employs a laser as the energy source, with powder feedstock blown using inert gas into a melt pool to form deposited beads of material. The process involves a blown powder deposition head and laser beam optics that are mounted on a gantry or robot [32]. This setup enables the required accuracy in motion control to manufacture components featuring 1 mm thick walls and integral microchannels (~2.5 mm) at diameters greater than 1 m [5,33]. While both LP-DED and L-PBF can be used to fabricate microchannel heat exchangers, a significant challenge for their implementation lies in achieving the required surface finish. It is widely acknowledged parts produced using AM have unique surface texture in comparison to traditional manufacturing methods [34,35]. Surface texture, in the form of roughness and waviness, is a critical geometric attribute in the design process, as it has the potential to influence mechanical properties such as fatigue life. Additionally, the surface quality has a significant influence on heat transfer and fluid flow efficiency. As AM is being used for many applications involving fluid flow, the characterisation of various AM processes and materials becomes critical for the industrialisation of these technologies. As the complexity and design potential of AM build processes continue to grow, post-processing steps such as heat treatments, machining, cleaning, inspections, joining, and surface enhancements are becoming critical to satisfy design and safety requirements [36,37].

Surface enhancements, often referred to as polishing or surface finishing, modify the profile of the surface to remove partially adhered powder particles, waviness, pores, defects, or other surface anomalies resulting from the AM process. Several review papers provide overviews about surface finishing techniques for AM parts [37–41]. Many mechanical and chemical processes, laser-treatments, and coatings that modify the surface without removing material, are discussed in the literature. These processes are often used to improve the fatigue life [42]. Many processes for finishing surfaces

require line of sight and access for tooling and are limited to external surfaces. These include machining, grinding, vibratory finishing, grit or sand blasting, laser polishing, rolling, burnishing, and peening [43–45]. A limited number of surface enhancement processes are feasible or hold potential for altering internal surfaces, and more so microchannels. These common processes include chemical milling, electro or electrochemical polishing, abrasive flow machining, chemical mechanical polishing, thermal energy method, and self-terminating sensitisation [42,46–49]. Other methods, like hydrodynamic cavitation abrasive finishing [50,51] and magnetic assisted finishing [52,53] have been studied for internal channels. However, these approaches have limited applicability and lack industrialisation.

Chemical milling (CM) and chemical mechanical polishing (CMP) are especially suitable for internal surfaces, more so if the geometry is intricate, because chemical solutions can flow through small and complex channels [54]. Favero et al. conducted a study applying the CM process using copper chloride and ferric chloride as the chemical solution to finish the internal surface of vertically built L-PBF pure copper channels with various internal geometries and a wetting length of 54 mm [55]. Their experimental findings revealed a reduction in the average areal roughness (Sa) by 83%, with a subsequent pressure drop decrease of 78%. However, the study did not delve into a detailed discussion of the specific mechanisms of the altered surface texture that resulted in the reduced pressure drop. Tyagi also evaluated acid-based chemical milling to reduce the average directional roughness (Ra) of an internal surface by 91% [56]. Limited public data exist for CMP, or chemical abrasive polishing. Mohammadian et al. demonstrated the possibility of polishing internal wedges of Inconel 625 channels made with L-PBF using a custom CMP setup [57]. A reduction of Ra by 44% and 18% was observed, based on build orientations of 15° and 135°, respectively. Other literature discussed the use of CM and CMP for surface modification of L-PBF channels, but comprehensive investigations regarding these surface modifications remain limited [6,58–63].

Min et al. evaluated electrochemical polishing (ECP) for Inconel 718 alloy built with L-PBF that included 500 µm holes [64]. A study by Jiang et al. was focused on the use of ECP to polish the inside of 3 mm diameter Hastelloy X channels produced by means of L-PBF. The results indicated an 83% reduction in Ra, but selective dissolution of the cellular structure and dependency on surface build orientation was observed [65]. An et al. demonstrated the use of combined electrochemical and mechanical polishing (ECMP) to finish the internal surface of channels with diameters as small as

18 mm and obtained a reduction of the Sa by 79.9% [66]. One limitation of this procedure is that the geometry must be simple enough to accommodate an electrode [54,67].

Ferchow et al. used abrasive flow machining to polish 6 mm diameter internal channels produced using L-PBF, by removing a maximum of 0.33 mm of material and thus reducing the Ra from 27.7 to 5.5 µm [68]. In another study [69], similar results are reported, but using AFM to improve the surface finishing of 8 mm diameter channels made of Inconel 718 and by means of L-PBF; in this case the Ra was reduced by 93%. Han et al. researched the application of AFM to polish 3 mm diameter maraging steel channels made with L-PBF and reduced the Sa from 7.6 to 1.3 µm. The peak regions were removed, but some valleys still remained [70]. Additional studies about the use of AFM for the surface finishing of internal channels were conducted and all concluded that the removal of surface peaks was prevalent but valleys remained [40].

The surface enhancement methods for internal channels detailed here were tested only on parts manufactured with L-PBF, while the use of these surface finishing technologies in association with parts obtained with the LP-DED process is not documented. Researchers have noted that geometry, AM processing, feedstock, microstructure, and heat treatments can all effect postprocessing such as surface finishing [71]. Detailed conclusions about surface finishing methods cannot be generalised to different AM processes, alloys, and geometries. If the level of finishing of internal surfaces of microchannels obtained with AM is insufficient to attain the desired flow resistance or fatigue life, then an additional finishing process is required to modify the surface geometry and roughness and to remove defects. However, detailed research must be conducted for each AM process and material of interest.

This work is about the experimental characterisation and test results of surface enhancement methods applied to microchannels produced using the LP-DED process. These enhancements included abrasive flow machining, chemical milling, chemical mechanical polishing, pulsed electrochemical machining, and the thermal energy method. These processes were applied to modify the internal surfaces of LP-DED microchannels built using a hydrogen-resistant NASA HR-1 alloy. This research addresses a notable knowledge gap, as microchannels created using LP-DED have limited data available [5], and research on the improvement of finishing of their internal surfaces is limited. This work involved a comprehensive characterisation of the surface texture, using scanning electron microscopy (SEM), optical microscopy, and computed

tomography (CT). Hydraulic flow testing was conducted to assess discharge coefficients and provide comparisons between each of the surface enhancement processes. The discharge coefficient was used as a quantitative measure to determine flow resistance in microchannels, considering variations in surface texture. The research objective was to characterise the various surface enhancement methods and their impact on flow resistance, focusing on evaluation rather than optimisation for a 'smooth' surface. These various surface conditions may, in turn, allow designers to fine-tune these surfaces to meet specific requirements of end-use applications. This potential extends to leveraging additive manufacturing to balance factors including heat transfer, fluid flow friction, corrosion, mechanical fatigue life, and aesthetics.

## 2. Methodology

Several channel samples were built using the LP-DED process. Surface enhancements were used to modify the internal perimeter of the channels. These channel samples were flow tested to determine the discharge coefficients of each channel. Following testing, the channel samples were sectioned to characterise the internal surface and flow area to anchor the test data.

### 2.1. Fabrication of DED samples and processing

The channels were designed with a nominal width and height of 2.54×2.54 mm square and built using LP-DED. Figure 1 illustrates the LP-DED build and subsequent processing of the channel samples. The length of the square microchannel section was approximately 150 mm. A 25 mm blended transition from the square channel to a round extrusion was designed to allow welding of a universal AN-type fitting as shown in Figure 1D. The channels were built as part of larger sample boxes (Figure 1(B)) using the NASA HR-1 alloy and then individually sectioned (Figure 1(C and D)). This Fe-Ni-Cr superalloy is resistant to hydrogen environment embrittlement (HEE) in high pressure components [31]. It was developed for high strength and high ductility in harsh hydrogen environments, like those occurring in liquid rocket engine nozzles and heat exchangers. It is derived from the A-286 and JBK-75 alloys [28,72]. The boxes were built with an RPM Innovations (RPMI) 557 LP-DED machine equipped with an argon-inert build chamber (Figure 1(A)). The 557 system incorporated an infrared (IR) continuous-wave gaussian profile 3 kW IPG laser, three coaxial powder injection nozzles within the deposition head, 5-axis motion control, and disc powder feeder with agitation

capabilities. The samples were built on top of an A36 mild steel 12 mm thick base plate. The laser power was 350 W, with powder feed rate of 23 grams/min, a travel speed of 763 mm/min and a layer height of 0.254 mm. Based on previous development work, this set of parameters was optimised to produce crack-free material, resulting in very low porosity [73,74].

The powder was rotary atomised by Homogenized Metals Inc. (HMI), with a particle size distribution (PSD) of 55–105 μm meeting +140 mesh at 0% and −325 mesh at 3.8% per ASTM B214 using a Microtrac (Ver 11.1.0.6). The chemical composition is listed in Table 1 (HMI powder lot HRA4). The Oxygen content was 61 ppm and the Nitrogen content was 7 ppm. The chemical composition was measured using Inductively Coupled Plasma (ICP). The peak powder size was 70 μm and a Vega3 Tescan Scanning Electron Microscope (SEM) using Backscatter Electron (BSE) showed mostly spherical particles with a few satellites and random distribution of occasional oblong particles. Virgin powder was used for all builds.

The sample channel boxes were stress-relieved at 1066°C for 90 min with a slow furnace cooling, prior to removal from the build plate with a bandsaw (Figure 1 (B)). The boxes were then homogenised at 1163°C for 6 h in vacuum and Argon-quenched. A solution anneal was performed at 1066°C for 60 min, with an Argon-quench followed by age-hardening at 690°C for 16 h. The boxes were then furnace cooled to 621°C and held for 16 h (total aging time of 32 h) [33,75]. Individual channel samples were then sectioned from the boxes using a water jet (Figure 1(C)). The samples were cleaned and an AS5174-04 stainless steel fitting was laser welded to the inlet end of the samples (Figure 1 (D)). The channels were labelled according to the surface enhancement processes. Several samples were used for process development and not tested. The internal surfaces of the channels were processed according to surface enhancements described in section 2.2. Following the polishing of the internal perimeter, a 0.75 mm diameter hole was drilled at two locations and a 3.175 mm diameter tube was welded as shown in Figure 1E.

### 2.2. Surface enhancement processes

Several internal surface enhancement processes were selected with the ultimate goal of testing the possibilities of improving the flow friction characteristics of heat exchanger channels. These included abrasive flow machining (AFM), chemical mechanical polishing (CMP), chemical milling (CM), pulsed electrochemical machining (PECM), and thermal energy method (TEM)
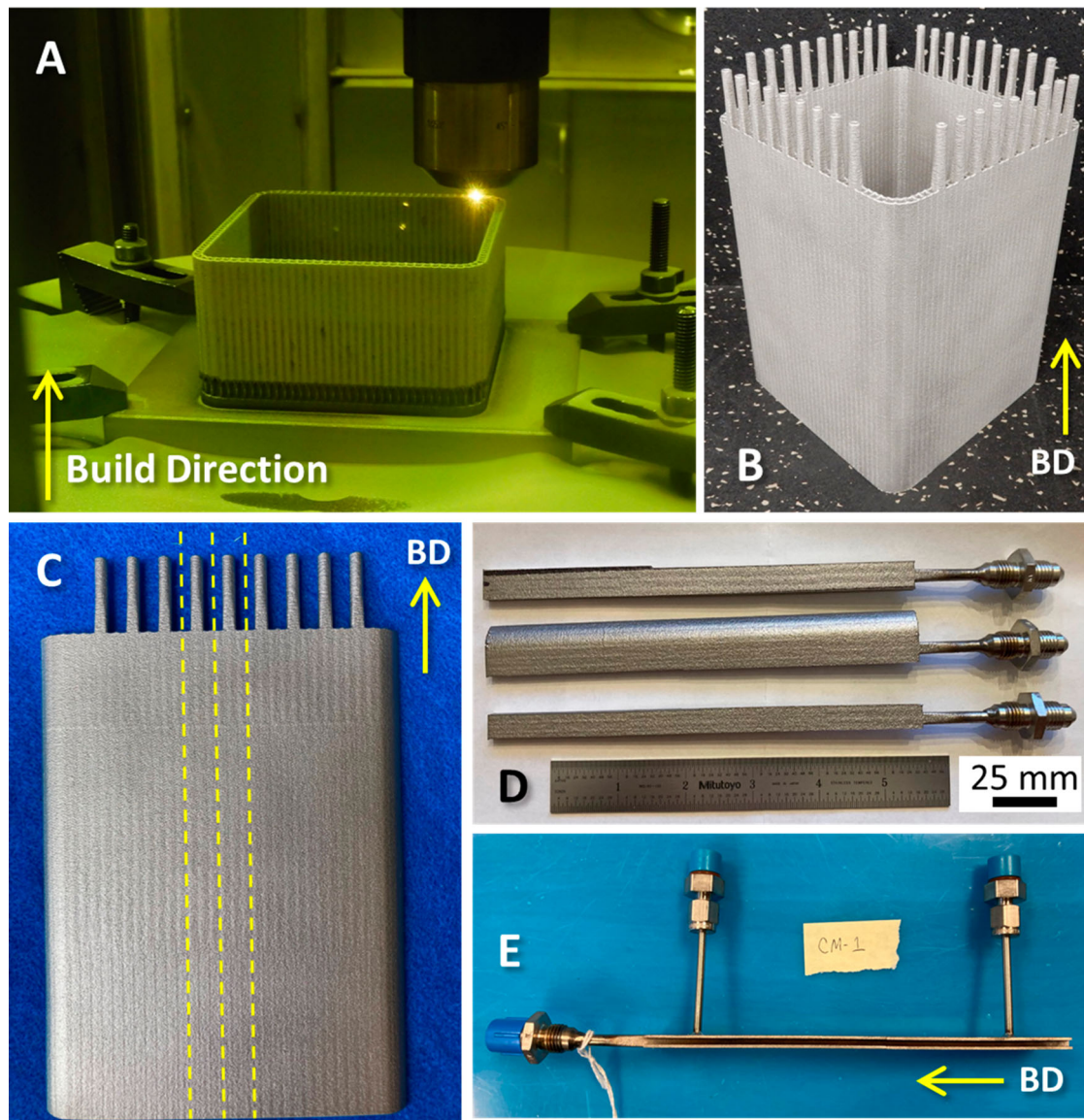
**Figure 1.** Channel specimen fabrication: (A) LP-DED of channel sample boxes, (B) complete NASA HR-1 box after stress relief and sectioning from the build plate, (C) Panels excised from boxes, (D) Individual channel samples with welded inlet port, and (E) drilled and welded instrumentation ports. Build Direction (BD) shown with arrow.

**Table 1.** Chemical composition of NASA HR-1 alloy powder (HMI Lot HRA4).

|  | Fe | Ni | Cr | Co | Mo | Ti | Al | V | W |
|---|---|---|---|---|---|---|---|---|---|
| Wt. % | Bal. | 33.71 | 14.49 | 3.75 | 1.82 | 2.31 | 0.24 | 0.3 | 1.59 |

or thermal deburring. These enhancement processes were selected among the many available [37,44,47,76,77], based on the ability to modify internal microchannels with a cross section of less than 2.54×2.54 mm [42,46,63,78]. The primary goal of this research was not to minimise surface roughness or to allow for the best possible surface polishing of the channels, but to analyse the varying levels of surface polishing that can be obtained to gain a better understanding of how the polishing can be tuned to the requirements in terms of flow resistance.

AFM uses a viscous fluid polymer that contains suspended abrasive particles. The slurry is pressurised and pumped through the channels using a single or bi-directional flow [79,80], thus providing abrasion, and the removed particulate is carried away with the media. This process is also referred to as *extrude-honing* or *slurry-honing*. The slurry type, volume, time, and

number of cycles were adjusted to modify the channel surfaces. The pressure was 68.9 bar and the flow was unidirectional and the flow rate ranged from 0.56 L/min to 4.47 L/min. Following the AFM process, the slurry was removed with compressed air and rinsed with a cleaning solution. The channels were then dried with compressed air, ultrasonically cleaned, rinsed with water, and again dried.

CM, or chemical polishing, consists of flowing a chemical solution through the channels that attacks the grain structure and dissolves the metal at the surface [81,82]. The dissolved material is flushed out with the hydrofluoric solution. Longer exposure times yield more material removal. The temperature of the solution pumped through the channels varied from 52°C to 60°C and the surfaces were exposed to the solution for a period that ranges from 4 to 19 mins. The parts were rinsed following the chemical milling.

CMP is a process in which chemical and mechanical forces are applied to remove surface material along preferential directions thus reducing the peak height [83]. The chemical solution removes most of the material, while abrasive media planarises the surface. The chemical solution and micro-abrasives were flowed through the channels and any removed particles flushed with the solution. The flow rate of the chemical solution, temperature, time of flow, and weight of the microabrasives was varied for each channel. The flow rate was varied from 0.4 to 2 L/min at temperatures of 50°C to 60°C and runs with and without microabrasives (up to 10%). The exposure time was also varied between 10 to 20 mins.

PECM obtains the surface improvement by applying a local direct current (DC) pulse using an electrode to dissolve metal [84]. The electrode was inserted inside of the channel and dragged through, thus providing the proper offset gap. A limited portion of the electrode was exposed. The channel was actively flushed with an electrolytic sodium chloride solution.

TEM is a process where parts are placed in a sealed chamber, which is pressurised with a mixture of gaseous fuel and oxygen, and ignited [85,86]. The high temperature of the combustion process vapourises (thin) areas with low thermal mass. The part was fixtured to prevent damage in the 25 cm diameter chamber operating at a combustion pressure of 6 bar with a total processing time of 30 s.

The surface enhancement processes were outsourced to commercial vendors actively working production. Prior to conducting the flow testing and characterisation, each vendor received development samples for trials. This step was necessary because both material composition and geometry can influence the parameters used. Although general parameters were outlined above in Section 2.2, detailed parameters and specific setups for each of the channel samples were deemed proprietary to the vendors. The objective of this research was to introduce variations in the surfaces of the channels rather than achieving an ideally 'smooth' surface. To meet this objective, vendors employed distinct parameter sets for each tube to generate the data for this study. The general setup of the surface enhancement processes is illustrated in Figure 2.

## 2.3. Test configuration and procedures

Testing was conducted at the NASA Marshall Space Flight Center component development facility. A 379-liter $GN_2$ pressurised tank provided deionised (DI) water to the system depicted in Figure 3. A 10 μm filter was placed immediately downstream of the tank after the main valve. A Potter Aero RAA-1/2-301-1/2-5440A flowmeter (3.4 to 36 l/min) was installed in a bypass leg of the system in addition to a 1.143 mm diameter cavitating venturi (Cd = 0.980) to control the mass flow through the channel test articles. The venturi cross-sectional area was sized to be smaller than the smallest cross-section area of the test article. Pressure and temperature measurements were installed at locations indicated on the diagram of Figure 3 and on the channel test article. The test article was installed in a blast containment due to the operating pressures. The Sensotech A-105 pressure transducers (0 to 40 bar, ±0.1% full scale), Omega E type thermocouples (−200 to 900°C ±1.7°C), flowmeter, and cavitating venturi were all calibrated prior to testing. Instrumentation checks were completed each day of testing.

Each channel test article was flushed with DI water at 7 bar for a minimum of 10 s prior to data collection. The tank was then pressurised at increments of 34, 69, 138 bar and held for 10 s at each pressure. The selected pressures were based on the maximum allowable tank pressure, whose value is of the same order of magnitude of the pressure at which high-pressure heat exchangers are operated (e.g. rocket nozzles, components of power and propulsion systems). A Dewetron data acquisition system was used in conjunction with the LabVIEW software for system control. Following pressurisation of the test articles at the three set points, all pressure in the system was vented and a new test article installed. A total of 20 channel samples were tested (Table 2). Each sample was uniquely numbered based on the processing (AB = As-built; AFM = abrasive flow machining; CM = chemical milling; CMP = chemical mechanical polishing; PECM = pulsed electrochemical machining; TEM = thermal energy method).
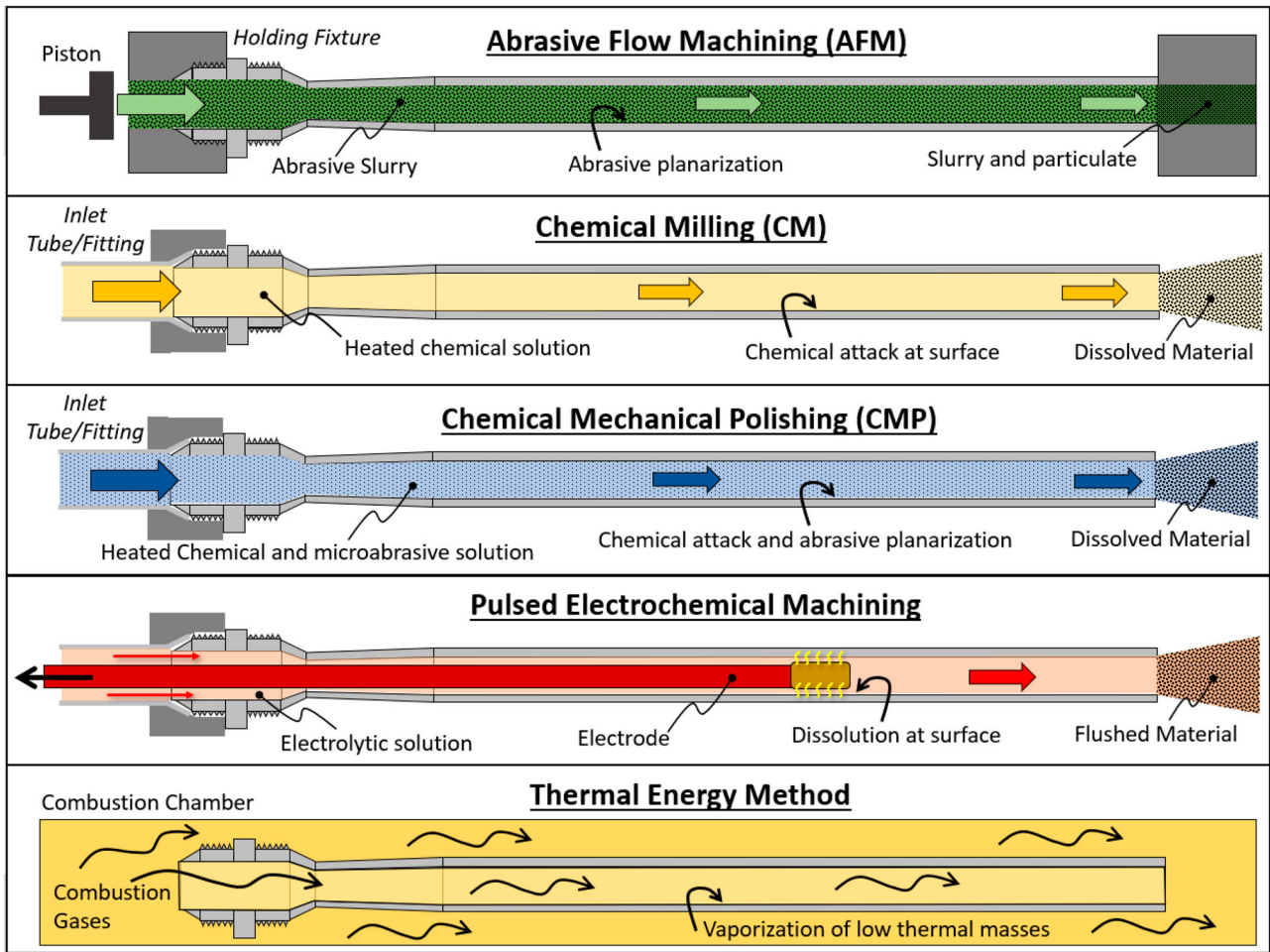
**Figure 2.** Overview of surface enhancement processes used for internal LP-DED microchannel samples.
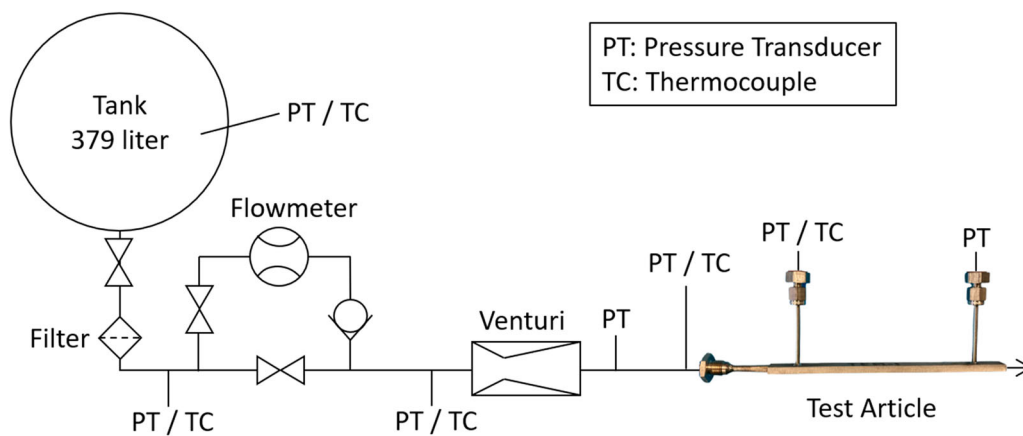


**Figure 3.** Flow test configuration.

## 2.4. Sectioning and imaging

Following flow testing, the channel samples were sectioned to characterise the channel geometry and surfaces using optical microscopy, optical imaging surface texture, SEM imaging, and computed tomography.

### 2.4.1 Optical images

Each channel sample was cross sectioned at three axial locations perpendicular to the flow (Figure 4). The samples were mounted and polished according to the ASTM E3 standard using a Presi automatic polisher. The samples were polished using 0.5 μm colloidal silica

**Table 2.** Optical and SEM image geometric measurement and discharge coefficient results and standard deviations.

| Sample ID | Perimeter (mm) | Area (mm$^2$) | Area Change from AB-Avg (%) | Material Removed (µm per side) | Avg Particles (per mm$^2$) | Cd, Actual | Cd Change from AB-2 (%) |
|---|---|---|---|---|---|---|---|
| AB-2 | 13.36 ± 0.45 | 6.19 ± 0.038 | −0.8% | 0 | 98 ± 1 | 0.44 ± 0.004 | 0.0% |
| AB-3 | 13.45 ± 0.18 | 6.30 ± 0.038 | 0.8% | 0 | 93 | 0.43 ± 0.007 | −1.9% |
| AFM-2 | 10.87 ± 0.12 | 6.85 ± 0.027 | 9.7% | 88 ± 9.4 | 0 | 0.85 ± 0.002 | 92.9% |
| AFM-7 | 10.64 ± 0.12 | 6.97 ± 0.059 | 11.7% | 87 ± 16.7 | 2 | 0.88 ± 0.003 | 98.8% |
| AFM-15 | 11.64 ± 0.19 | 6.37 ± 0.050 | 2.0% | 41 ± 8.0 | 18 ± 0.5 | 0.59 ± 0.004 | 34.0% |
| AFM-16 | 11.33 ± 0.11 | 6.53 ± 0.059 | 4.6% | 51 ± 14.0 | 2 | 0.71 ± 0.003 | 60.7% |
| AFM-17 | 11.28 ± 0.40 | 6.67 ± 0.094 | 6.9% | 61 ± 14.6 | 0 | 0.75 ± 0.002 | 70.5% |
| CM-1 | 11.52 ± 0.04 | 7.36 ± 0.077 | 17.9% | 85 ± 14.3 | 5 ± 1 | 0.76 ± 0.011 | 73.4% |
| CM-3 | 11.54 ± 0.10 | 7.24 ± 0.015 | 16.1% | 97 ± 13.0 | 4 ± 1.5 | 0.76 ± 0.023 | 73.1% |
| CM-9 | 11.37 ± 0.06 | 7.29 ± 0.136 | 16.8% | 121 ± 17.2 | 3 ± 1 | 0.75 ± 0.018 | 69.6% |
| CM-16 | 11.98 ± 0.12 | 8.28 ± 0.214 | 32.8% | 207 ± 12.8 | 2 | 0.94 ± 0.017 | 113.5% |
| CM-17 | 12.20 ± 0.18 | 8.20 ± 0.170 | 31.6% | 197 ± 16.1 | 1 | 0.85 ± 0.032 | 92.8% |
| CM-20 | 12.06 ± 0.03 | 8.50 ± 0.032 | 36.4% | 213 ± 18.1 | 1 ± 0.5 | 0.97 ± 0.016 | 120.7% |
| TEM-1 | 13.45 ± 0.39 | 6.28 ± 0.102 | 0.6% | 17 ± 7.0 | 87 | 0.44 ± 0.005 | −0.9% |
| PECM-1 | 12.55 ± 0.50 | 6.53 ± 0.035 | 4.6% | 61 ± 16.6 | 3 ± 0.5 | 0.55 ± 0.006 | 26.0% |
| PECM-9 | 12.02 ± 0.25 | 6.47 ± 0.211 | 3.6% | 47 ± 14.0 | 2 | 0.55 ± 0.009 | 24.3% |
| CMP-1 | 12.14 ± 0.29 | 6.75 ± 0.049 | 8.1% | 62 ± 15.3 | 0 | 0.50 ± 0.005 | 13.5% |
| CMP-2 | 11.31 ± 0.37 | 6.89 ± 0.208 | 10.4% | 53 ± 11.3 | 8 | 0.81± 0.010 | 83.4% |
| CMP-6 | 11.97 ± 0.07 | 7.94 ± 0.083 | 27.3% | 162 ± 17.3 | 6 | 0.89 ± 0.024 | 103.0% |
| CMP-7 | 11.63 ± 0.13 | 6.82 ± 0.039 | 9.3% | 58 ± 12.9 | 8 ± 1 | 0.56 ± 0.007 | 26.7% |

and optical images obtained. Samples were then etched using etchant #13 (10% Oxalic Acid, Electrolytic) and optical imaging completed again. All optical images were obtained using a Keyence VHX digital microscope. The *Image J* image processing software [87] was used for analysis to obtain the cross sectional area and the wetting perimeter (Table 2). The porosity of each sample was also measured, and the results are provided in the supplementary materials. The results were averaged, and standard deviation reported from the three cross-sections. Each image was also overlayed to compare the processed sample to an as-built sample (identified as AB-2). These overlay images were used to measure the approximate amount of material removed per side, according to the hypothesis that the removal was uniform on all sides. The material removal was measured normal to the wall at 20 locations and data averaged. From the images, this hypothesis is only partially verified, since some surface enhancement processes removed more material in the centre of the channel wall as opposed to the corners. The perimeter of each channel was measured at the three axial locations and the average is reported.

### 2.4.2 SEM imaging
The surface perpendicular to the flow was imaged using a Hitachi S3000H Scanning Electron Microscope (SEM) (Figure 4). The particle count was determined by examining the number of particles in two 1 mm$^2$ areas and averaging (Table 2). This was obtained from the SEM image at 50x.

### 2.4.3 Surface texture measurements
Surface texture measurements were obtained using a non-contact Keyence VR-5200 pattern light projection profilometer. The setup included three telecentric
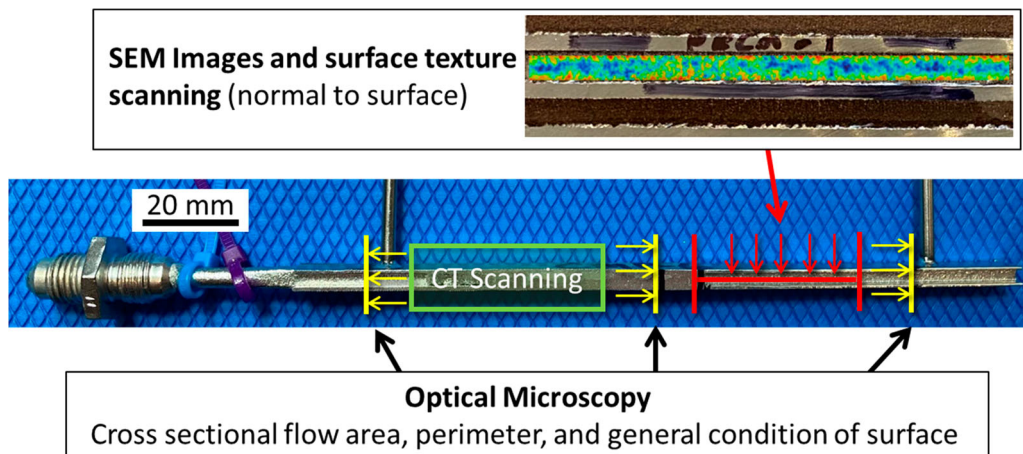


**Figure 4.** Sectioning of channels post-flow testing. An example scan of the areal surface texture is provided along the length of the channel.

lenses with 80x magnification capability and an overlap of 20%. An area approximately 38 mm long and 1.6 mm wide was measured for each sample. All areal surface measurements are reported according to ISO 25178-2:2021 [88,89]. The surface data intersecting the corners of the channels were eliminated using an end-effect correction. A surface form correction was applied to remove any tilt and curvature, addressing any residual stress distortion of the samples, and establishing a reference plane. For the areal surface measurements, the primary texture profile was left unfiltered (denoted as primary) using only the form correction. To extract roughness and waviness from the areal surface, a λc spatial frequency cut-off filter of 0.8 mm (i.e. a roughness filter) was applied following the ISO 21920-3 guidelines. To obtain directional roughness and waviness (i.e. Ra and Wa, respectively), a virtual line was created along the centre of the channel, and data were extracted to report the results. Various areal data sets such as average texture (Sa), maximum surface height (Sz), core texture depth (Sk), reduced peak height (Spk), and roughness peak density (Spd) were obtained for evaluation based on prior literature [73]. Directional data sets for average roughness (Ra), average waviness (Wa), waviness peak height (Wp), and waviness peak density (WPc) were also evaluated along the direction of flow.

### 2.4.4 Computed tomography scanning

Micro-computed tomography (µCT) scanning was completed on seven samples including AB-2, AFM-2, AFM-15, CM3-, CM-20, PECM-1, and CM-20. These samples were selected to evaluate each of the surface enhancement processes and the range of the calculated discharge coefficient. A fully intact 17 mm length portion of the channel samples were CT-scanned as shown in Figure 4. The specimens were scanned on a Zeiss Xradia Versa 620 using 159 kV and 23W and exposure of 8.7 s. A variable exposure scan technique was employed to help reduce noise while simultaneously reducing the overall scan duration. The imaging covered an area of 19 mm$^2$ per scan and the estimated pixel size is 10.03 µm. This resulted in a feature resolution of ~30 µm, which is typically 3–5 times the pixel size [90].

## 3. Results and discussion

### 3.1. Image analysis

#### 3.1.1 Optical images

The cross sections of each channel are documented in Figure 5. The channel cross section is overlayed with the AB-2 channel coloured in grey, while the removed material is depicted in orange. The AB-2 channel sample was used as the baseline since this is unprocessed. These micrographs were obtained at the first pressure port on the test article. The images were used to determine the area, perimeter, and approximate thickness of the removed material, per side. The as-built sample displays pronounced texturing due to excessive powder adherence and disturbances of the melt pool [73]. This texturing increases the wetting perimeter by 32% compared to the as-designed (nominal) channel. Corners are created at the intersection of the melt pool solidification with the upper and lower walls extending to the intersecting ribs (depicted vertically in Figure 5). A minor thickness increase is noticeable at the mid-span centre of the ribs, accompanied by a gradual thinning of the ribs as they approach the upper and lower walls. This is the region where the laser is triggered off to prevent excessive material deposition at the wall intersections.

All samples were crack free and the microstructure of the samples was identical to 1 mm thick walls evaluated in prior studies [73,74]. The grain structure is shown to be fully homogenised. The average porosity across all samples was 0.042% with a maximum porosity of 0.108% on sample CMP-1 due to a single pore in the bulk of the material. The polished and etched sample images are shown in supplemental and a table with the measured porosity for each sample.

Varying degrees of material removal were present on all samples, as expected since this was one of the objectives of the experiment. The cross-section micrographs reveal that the walls of the AFM samples exhibit a visually smooth surface. The internal area increased in comparison to the as-built channel by as much as 2% to 12% across the different AFM samples, and the perimeter increased up to 15% compared to the nominal design. The corners indicate sharp stress risers, revealing that abrasive machining was less effective in the corners. The AFM process selectively removed material from the mid-span thickness of the ribs. This resulted in nearly flat ribs with some AFM walls showing concavity. The AFM overlay with the as-built sample confirms the selective material removal in the rib mid-span and no removal in the corners.

The internal surfaces of chemically milled samples are larger compared to that of the other samples and the corners are fully rounded. The walls appear jagged at high magnification and much smoother as more material is removed. This is due to the milling solution following the as-built profile of the surface. The area increased by 16% to 36% if compared to the as-built state depending on the CM sample, and the perimeter increased by 12 to 20% compared to the nominal
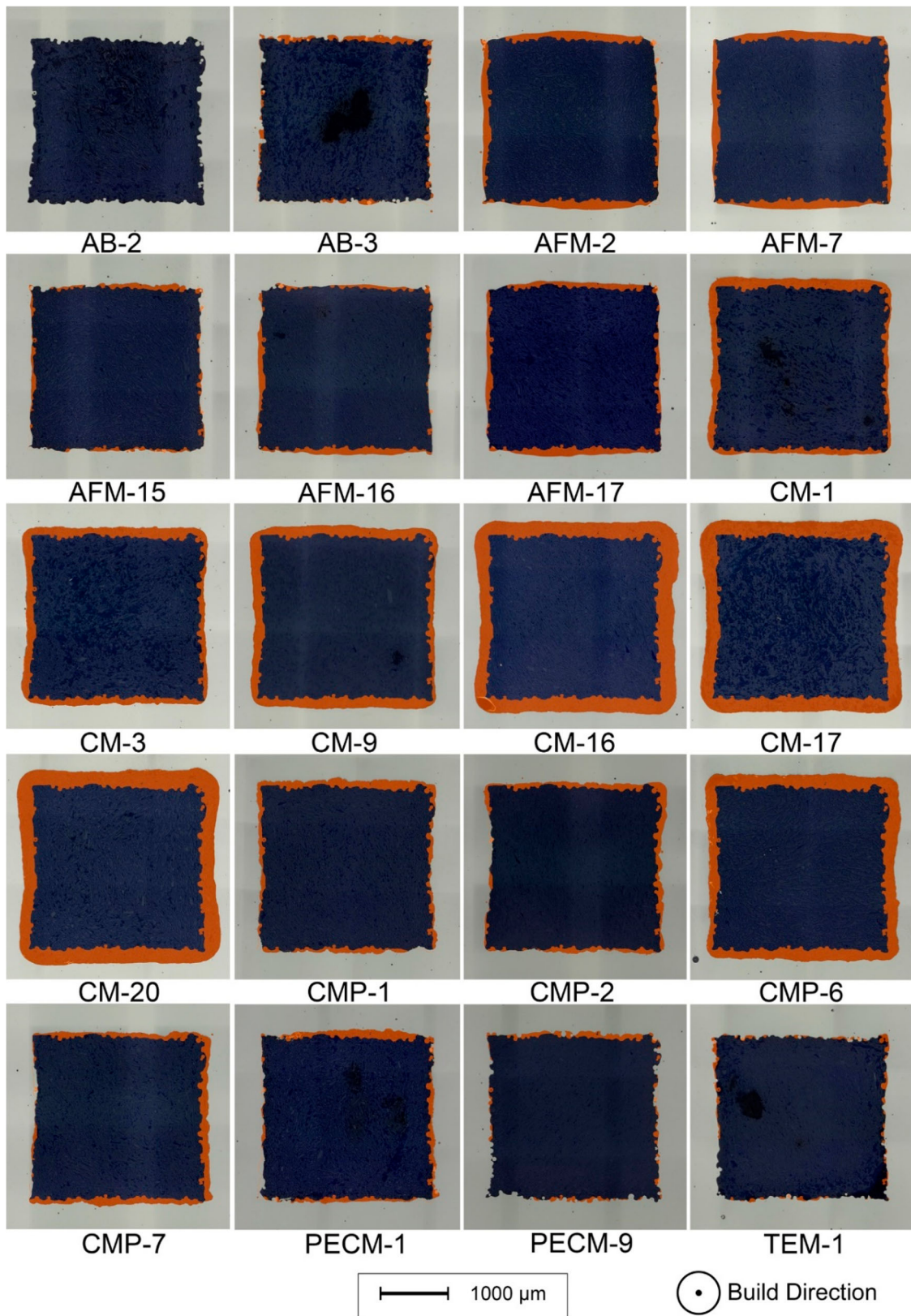
**Figure 5.** Polished cross section of channel samples incorporating an overlay of the section of an as-built (AB-2) channel (grey). Orange indicates the material removal from the sample.

design. The overlay images show that around the edges and corners the milling is uniform. The processing time for CM is the shortest and the surface changes are directly related to the increase of milling time and flow rate.

CMP allows for the removal of the widest range of material and therefore a wider control over the determination of the inner surface, as it allowed to obtain an area change spanning from 8 to 27%. At high magnification, the CMP samples revealed jagged features on the walls which gradually smoothed out as more material was removed. The perimeters were 11 to 19% larger compared to the nominal design perimeter of the channel. There were some remnants of residual powder with material removal uniform on the walls and corners. Visually, there appears to be a smooth wall profile indicating reduced texture. PECM cross sections indicate some removal of material from the walls, but the surfaces still show significant texture. There is no change to the corner geometry and perimeters increased (18 to 24%), indicating some reduction in material. The TEM sample does not exhibit any visual change compared to the as-built. The overlay with the as-built sample looks nearly identical and this observation is confirmed by perimeter and area measurements.

For all the surface enhancement processes, the increase in measured area is related to the amount of material removed per side. The perimeter length exceeds the design value and is notably influenced by the extent of powder adherence, as demonstrated by both the as-built and the TEM samples. Most processes eliminated the partially adhered powder particles except for TEM. Although a small number of residual particles persisted on the samples, a minimum material removal of 45 µm on each side is required to eliminate over 90% of the particles.

### 3.1.2 Scanning electron microscope

Figure 6 shows the SEM images of the inner surface samples, taken normal to the surface. The as-built samples indicate excessive powder adhered to the surface, previously reported to vary based on build angle and geometry [73]. The adhered powder particles were tallied per millimeter of area and averaged. The powder count for the AB-2 and AB-3 samples was similar, and that of TEM-1 was only slightly lower. Since the powder is partially melted into the solidified material, the TEM process does not provide sufficient energy to vapourise the material because the thermal mass is too much. The AFM samples reveal excess powder in the corners, which aligns to observations related to the micrograph of the cross sections. The visual SEM of the surface indicates some periodic texturing and varies with the

AFM parameters. The AFM-15 sample reveals a substantial amount of adhered powder that has been partially removed, leaving only a portion still attached. This indicates that not enough material was removed (41 µm). At higher SEM magnification (Figure 7), visible lines (i.e. scratches) are indicated in the direction of flow due to the abrasives in the slurry [91].

The CM samples are characterised by some jagged edges and irregularities, which are more visible at higher magnification. The surface texture also exhibits directionality, more pronounced in CM-9 and CM-17. The surface texture aligns with the chemical solution flowed, which is indicated explicitly in CM-17, where flow was disrupted by an adhered particle. Several remnant particles and crystals can also be observed along with some evidence of delamination of selected particles. The delamination is likely due to a partially adhered particle where a gap was present, and the chemical solution could flow.

The results of the CMP process are similar to those obtained with CM, whereby some surface directionality can be observed and it is due to the flow of the chemical solution. However, the jagged features observed on the surface of the CMP samples are coarser if compared to those visible on the surface of the CM samples and the surface is smooth, in general. The CMP-2 and CMP-6 samples indicate selective etching at grain boundaries, which is superficial, along with annealing twins. Some random micro-pitting is also present on the surface of the CMP samples, indicating that the material was over-exposed to the chemistry during processing. CMP-7 displays an uneven surface characterised by round particle and fractures. Some evidence of brittle fractures are observed and cleavage fractures which indicate the polishing media impacted and sheared loosely adhered powder particles.

The PECM process sample also illustrates micro-pitting, which is typical of corrosion when the electrolytic residues remain on the surface [92]. The surface characteristic are similar to those of surfaces obtained with L-PBF and finished with ECP, as documented in the work of An et al. [66]. A limited number of powder particles can be observed on the surface of the PECM samples. The centre of the channel exhibits less pitting than the edges near the sidewall due to the shape of the used electrode and to differences in local current.

### 3.1.3 Computer tomography

The selected samples that were µ-CT scanned (Figure 8) included AB-2, AFM-2, AFM-15, CM-3, CM-20, PECM-1, and CMP-6. The resulting images may not be fully representative of each of the corresponding processes since process parameters varied for each. The µ-CT data sets
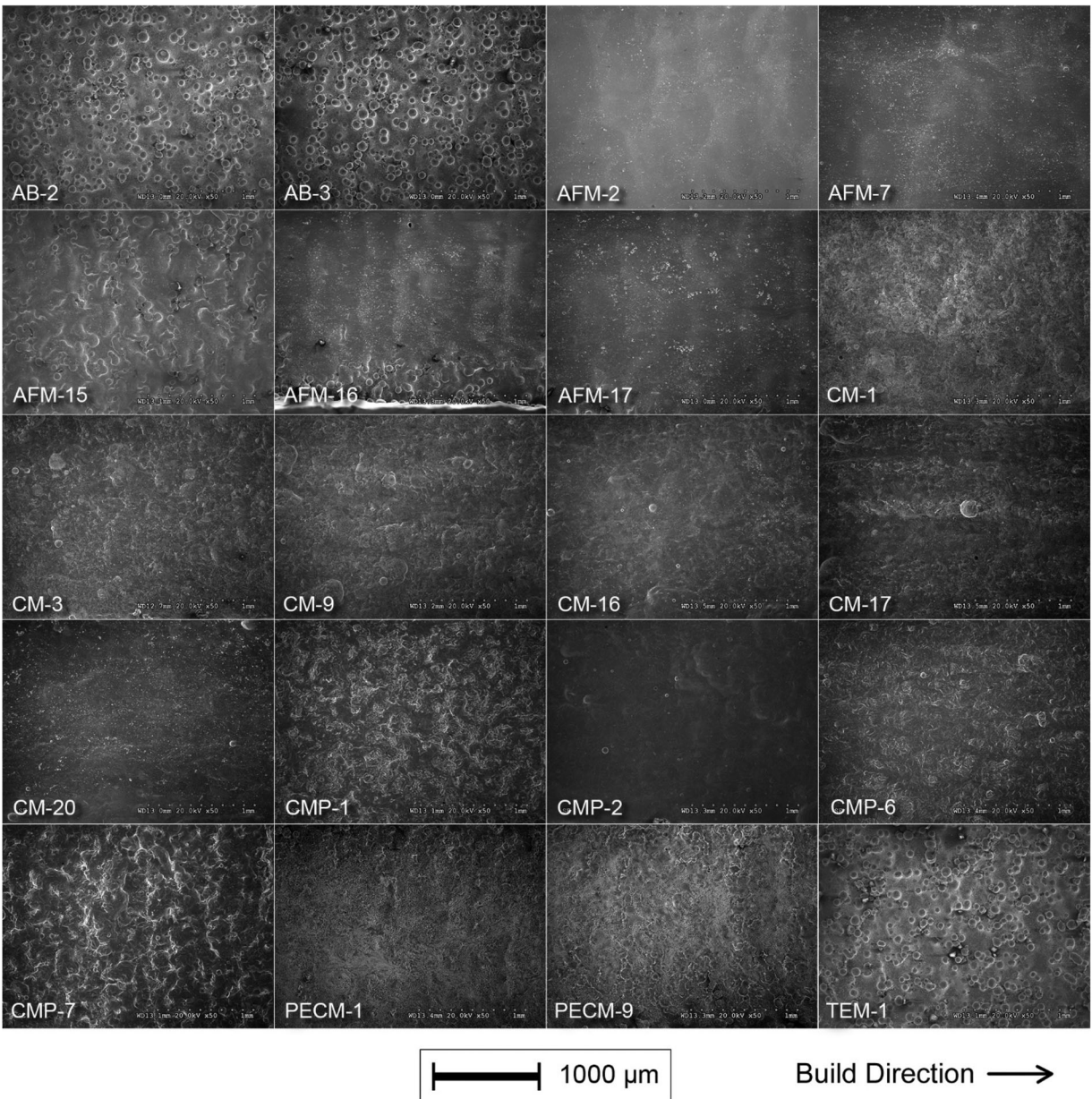
**Figure 6.** SEM 50x magnification images of the surface of each channel. Images are taken normal to the surface.

were reconstructed into a mesh with gaussian smoothing applied. The macro visual observations are similar to the optical and SEM images. The as-built samples indicate significant powder particle adherence. It is difficult to distinguish the corners and edge transitions and any potential waviness on the surface is masked by the high density of powder. The AFM-2 and AFM-15 samples show random particle adhesion with significant particle accumulation in the corners and waviness along the length. The periodicity of the waviness varies based on the sample.

The images of the CM-3 and CM-20 samples show significant rounding of the corners along with some waviness along the length. There are also some

indications of non-uniform material such as mid-points of the sidewalls. The PECM-1 sample exhibits fine roughness along the walls, which is smaller than the powder observed characterising the image of AB-2. There is a high density of powder in the corners and some indication of waviness along the length. The image of CMP-6 shows some indications of powder adherence and waviness along the length with a similar pattern to what can be observed in the image of CM-3.

### 3.2. Flow testing

A total of 60 tests were completed with three pressure settings for each of the 20 channel samples. The
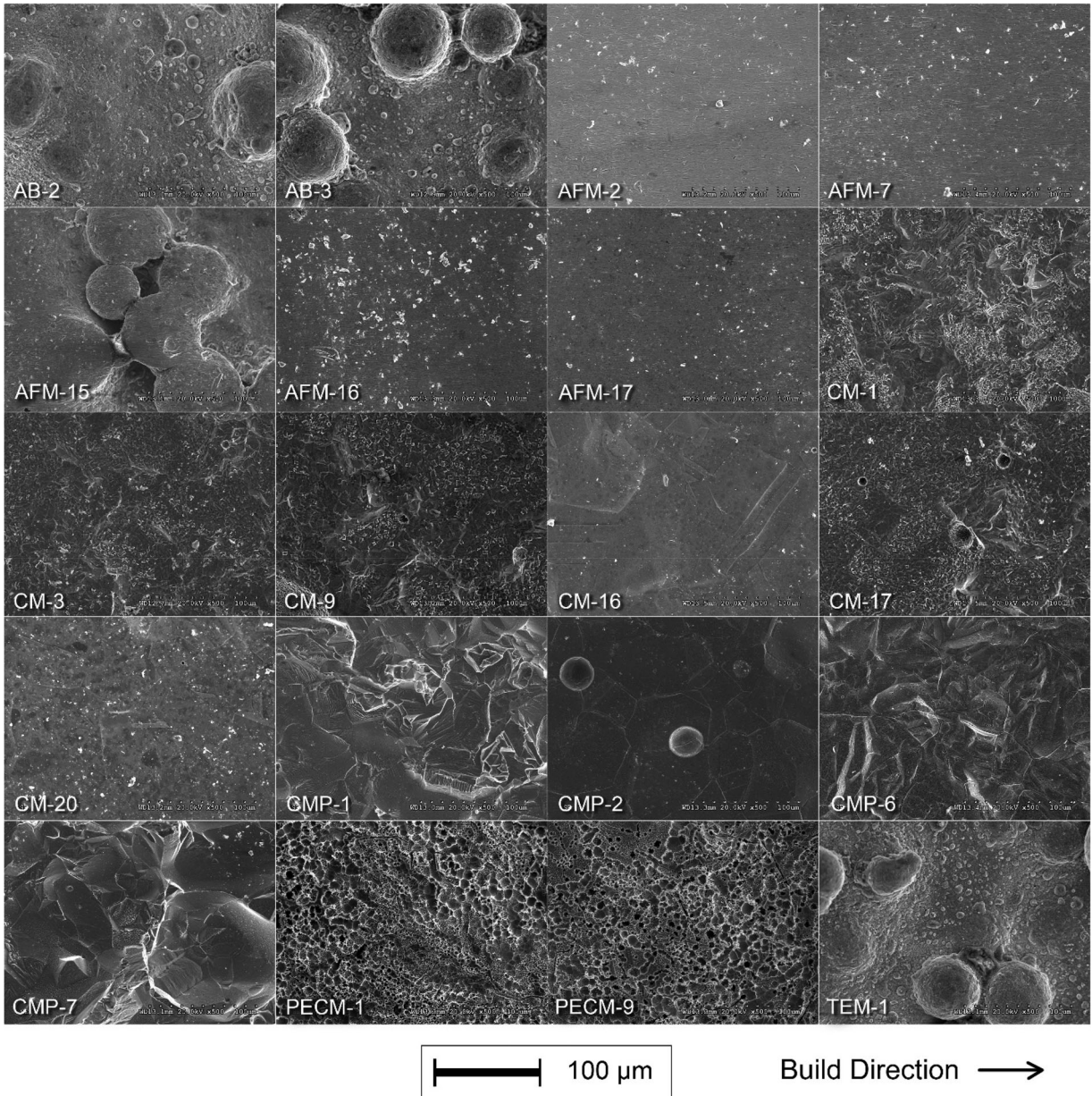
**Figure 7.** SEM 500x magnification images of the surface of each channel. Images are taken normal to the surface.

measurement results of the optical and SEM images are listed in Table 2 along with the calculated discharge coefficient (Cd). The Cd was used to establish a relative comparison of the various surfaces resulting due to the polishing processes and is calculated according to

$$Cd = \frac{\dot{m}}{A\sqrt{2\rho P}} \qquad (1)$$

where $\dot{m}$ is mass flow rate (gram/second), $A$ is area (mm$^2$), $\rho$ is density of the water (grams/cm$^3$), and $P$ is pressure (Bar) at the port.

The Cd is reported based on the actual measured area of the channels, and the standard deviation is computed from three distinct pressure runs conducted for each channel. The mass flow rate was based on the measured value. The variance between the flow rate calculated using the venturi and that measured by the flow meter was within a margin of less than 2% across all tests. The cavitation of the venturi was verified based on the exit pressure to inlet pressure ratio (<0.80) for each test run. The water mass flow rates remained uniform for each test, approximately measuring 85 ±0.0086, 118 ±0.0075, and 167 ±0.0078 g/sec corresponding to the respective tank pressures. The pressure and temperature data were taken from a 10 s period (100 samples/sec) and averaged. The change in area is calculated from the average of six measurements (AB-Avg) from the AB-2 and AB-3 channels.
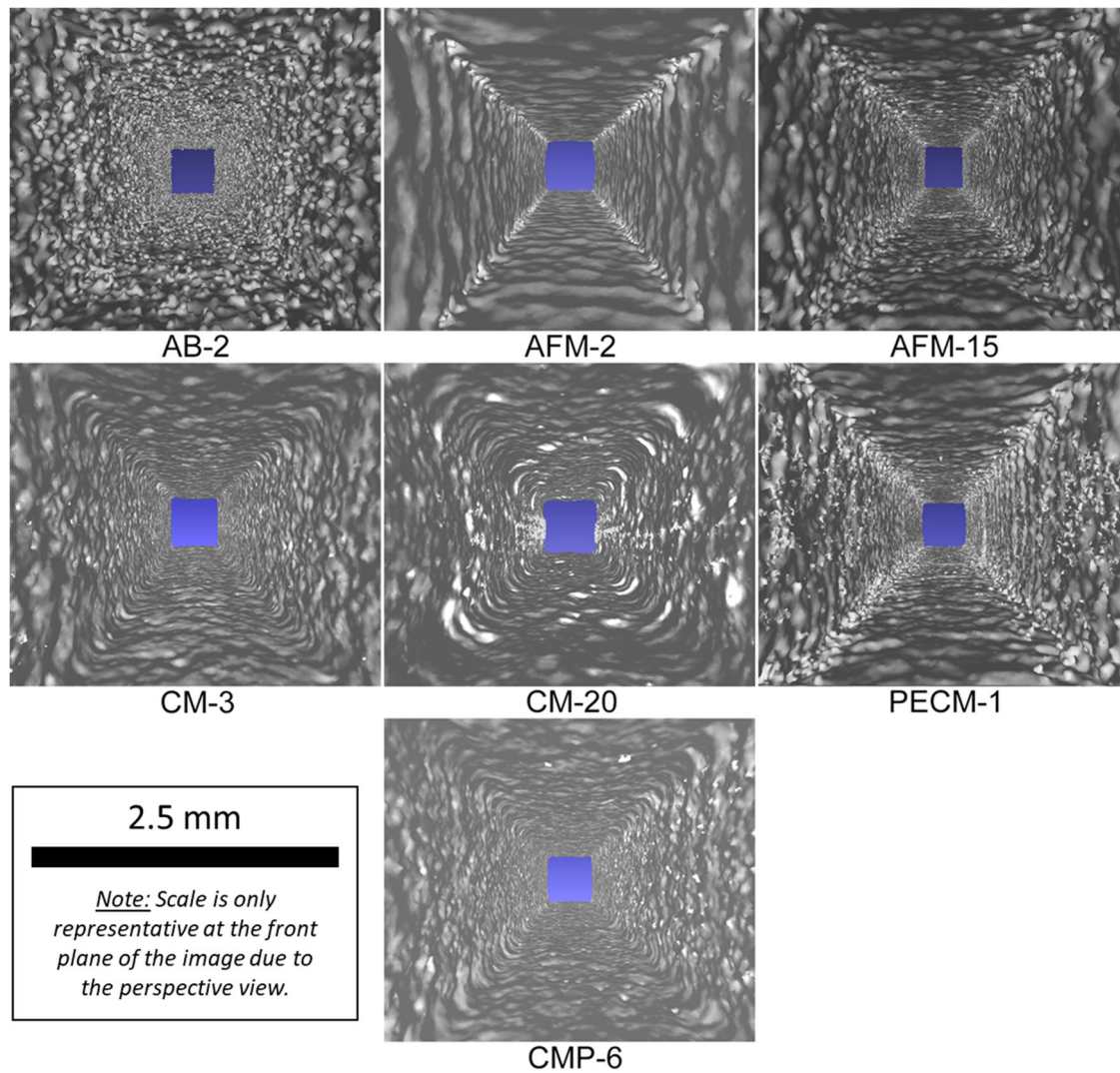
**Figure 8.** Micro-CT Scanning images related to various surface enhancement processes. The images are taken normal to the channel cross-section and looking in the same direction as the direction of the flow.

The discharge coefficient is plotted against measured cross-sectional area, measured perimeter, and average areal texture and depicted in Figure 9. The Cd is calculated using the measured area. At Cd below 0.6, the differences due to the as-designed (6.452 mm$^2$) to actual as-built area were minor. However, above a Cd of 0.7 when the nominal as-designed area is used to calculate Cd, it overpredicts its value since it is smaller than actual area (Supplemental). This is an important aspect related to additively manufactured surfaces since the actual as-built areas can be smaller due to powder adherence, melt pool irregularities, and droop and dross formation. The area of the CM samples increased by 36% resulting in a 120% change of the Cd. The as-built samples and the TEM samples featured the highest resistance, as expected, and the area value is smaller than the as-designed value by 4%. The obvious trend is the increase in cross sectional area due to the various processes resulting in larger Cd. However, for several channels with similar area, there were differences in the Cd. AFM-2, AFM-17, CMP-1, CMP-2, and CMP-7 all featured similar areas, but the Cd varies by more than 78%. Alternatively, comparable Cd values of around 0.9 were measured for AFM-2 and CM-17, despite a notable disparity in their cross-sectional areas, which differ by 19.7%. Similar cross-sectional areas were measured for AB-2, AB-3, TEM-1, and AFM-15, while AFM-15 is characterised by a higher Cd value. These variations can be attributed to differences in surface texture, perimeter, and the resulting resistance within the channel.

As the perimeter increases, the Cd generally decreases linearly. The larger perimeter, in the as-built samples, is caused by the partially adhered powder creating boundary layer turbulence and increased resistance [74]. The as-built perimeter is 30% larger than the
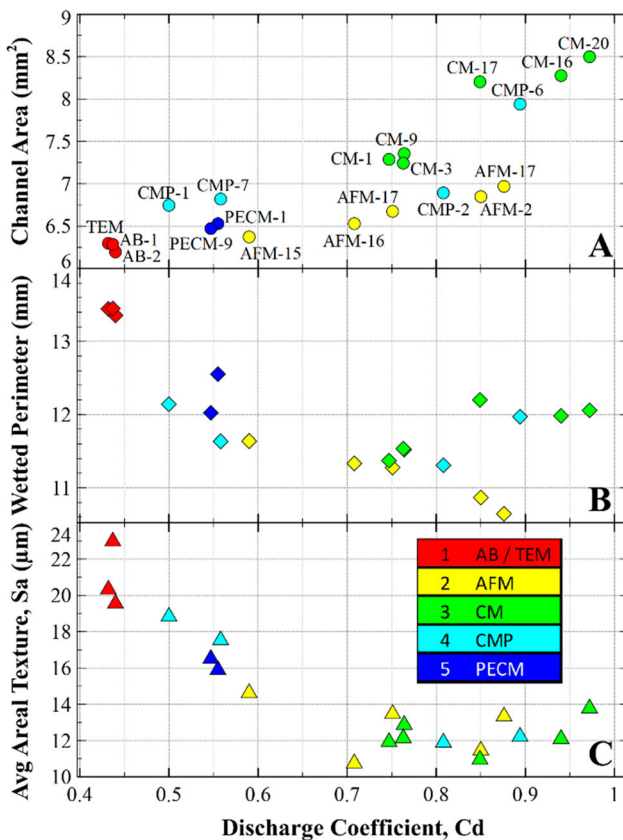
**Figure 9.** Summary of Cd and comparison to: (A) measured channel cross-sectional area, (B) measured perimeter, and (C) measured average areal texture, Sa. The data is coloured based on the surface enhancement process.

as-designed nominal perimeter. Figure 9B also depicts AFM-2 and AFM-7 among the smallest perimeters. This is due to the reduction of the sidewall texture, removing the mid-span rib material from the convex shape to flat. Additionally, there is powder remaining in the corners of several AFM samples creating a radius. This indicates the excess powder in the corners of the AFM samples did not have a significant impact on the Cd. There are a few outliers in perimeter plot, namely CM-16, CM-17, CM-20, and CMP-6. These outliers have lower average surface texture among the data set but their peculiar behaviour in the perimeter plot cannot be solely explained by the average Sa. There is an increase of Cd when the texture increases, as expected. There is a linear rise in Cd up to 0.6 based on a decrease of the surface texture. According to this data set, the surface texture below 14 µm plateaus although there is an increase in Cd.

Sa represents an average value and does not provide a comprehensive characterisation of the surface and its flow resistance. To gain a deeper insight into how surface texture impacts Cd, the data is evaluated based on the magnitude of the peaks and valleys and the density of these disturbances. While the maximum

height of the surface, denoted as Sz, can serve as a measure, it may not always accurately depict the true surface characteristics due to the presence of outliers, such as extremely elevated peaks or deep valleys. Sz, which sums the maximum peak height (Sp) and maximum valley depth (Sv), was compared to the Cd and no correlations were observed (Supplemental). This implies two key points: (1) the existence of anomalous localised peaks does not affect Cd, and (2) Sz is an inadequate measure to understand the surface texture mechanism influencing Cd. Instead, core roughness depth (Sk) is utilised as a substitute for Sz, representing the average peak-to-valley distance. The surface texture parameters discussed in this section are provided in Table 3.

Figure 10 shows that Sk reveals that as the peak-to-valley depth diminishes, Cd rises and then stabilises around a depth of approximately 40 µm. The peak height, referred to as reduced peak height (Spk), as indicated in Figure 10, illustrates that higher peaks contribute to greater resistance. For the samples featuring the highest Cd (CM-16 and CM-20), Spk constitutes roughly 8% of the surface, whereas it accounts for 13% in samples with lower Cd. The remaining portion of the surface comprises core roughness depth. Conversely, reduced valley depth (Svk) was assessed but no correlation was observed with Cd.

The roughness is due to powder adherence and melt pool irregularities. To better illustrate this relation, Figure 11 reports the average texture as a function of the average material removal per side in. The value of Cd is displayed as coloured dots whose shade is related to a scale. The value of Cd is consistently higher than 0.75 whenever and amount of sidewall material equivalent to the average powder size (70 µm) was removed. This led to a reduction in surface texture to values below 14 µm and is independent of the surface enhancement process. The results of these experiments revealed a strong variation of Cd if only the minimum powder size (55 µm) was removed, and limited discrete particles remained. According to particle count analysis, a material removal of 45 µm eliminated 90% of the adhered powder. However, this still resulted in higher Sa values due to remaining melt pool surface irregularities, which has an adverse impact on Cd. Particle density alone does not correlate with the Cd associated with the applied surface enhancement treatment. While material removal does play a role, its value alone cannot be used to predict the value of Cd. Certain processes, such as AFM, could achieve lower resistance with significantly less material removal if compared to that achievable with CM. For certain applications, the

**Table 3.** Summary of surface texture measurements.

| Sample ID | Primary Sa (µm) | Primary Sz (µm) | Primary Sk (µm) | Primary Spk (µm) | Spk, Lc=0.8 (µm) | Primary Spd (µm) | Wp, (µm) | WPc, (µm) | Ra, (µm) |
|---|---|---|---|---|---|---|---|---|---|
| AB-2 | 19.55 | 317.58 | 59.23 | 32.65 | 28.55 | 146.73 | 34.29 | 17 | 13.83 |
| AB-3 | 20.32 | 262.63 | 64.56 | 28.88 | 26.88 | 157.31 | 34.50 | 14 | 12.93 |
| AFM-2 | 11.45 | 177.42 | 35.82 | 15.19 | 7.12 | 469.99 | 24.72 | 15 | 4.60 |
| AFM-7 | 13.33 | 143.44 | 43.63 | 16.06 | 6.14 | 483.62 | 24.77 | 15 | 4.73 |
| AFM-15 | 14.62 | 223.05 | 45.82 | 18.58 | 12.02 | 248.58 | 36.69 | 15 | 9.85 |
| AFM-16 | 10.75 | 276.92 | 32.74 | 14.69 | 10.79 | 367.21 | 23.16 | 16 | 5.42 |
| AFM-17 | 12.87 | 144.62 | 40.37 | 12.64 | 7.45 | 380.05 | 29.77 | 8 | 4.84 |
| CM-1 | 12.14 | 227.75 | 36.51 | 12.46 | 8.97 | 414.75 | 26.81 | 9 | 5.06 |
| CM-3 | 11.92 | 216.35 | 38.27 | 12.75 | 7.96 | 403.73 | 24.29 | 9 | 4.54 |
| CM-9 | 13.47 | 257.08 | 42.23 | 17.46 | 9.67 | 394.85 | 29.81 | 13 | 4.88 |
| CM-16 | 12.09 | 250.73 | 38.68 | 11.16 | 10.74 | 344.90 | 22.35 | 10 | 5.60 |
| CM-17 | 10.95 | 225.53 | 34.46 | 12.35 | 8.14 | 463.47 | 23.47 | 7 | 4.30 |
| CM-20 | 13.78 | 373.49 | 40.51 | 10.91 | 12.13 | 452.59 | 23.12 | 8 | 3.48 |
| TEM-1 | 22.97 | 608.26 | 71.90 | 37.29 | 33.66 | 135.14 | 52.13 | 18 | 17.16 |
| PECM-1 | 15.89 | 216.56 | 49.90 | 24.59 | 12.77 | 335.47 | 30.24 | 14 | 7.11 |
| PECM-9 | 16.51 | 177.52 | 50.93 | 26.18 | 14.20 | 291.77 | 30.69 | 12 | 7.16 |
| CMP-1 | 18.83 | 382.78 | 59.37 | 22.58 | 17.24 | 351.23 | 42.19 | 13 | 10.53 |
| CMP-2 | 11.89 | 273.77 | 37.04 | 14.09 | 10.15 | 393.15 | 32.92 | 10 | 5.01 |
| CMP-6 | 12.21 | 231.75 | 38.70 | 14.54 | 8.43 | 493.41 | 22.77 | 12 | 5.44 |
| CMP-7 | 17.53 | 506.16 | 52.59 | 21.96 | 16.36 | 399.23 | 36.55 | 12 | 11.66 |

aim might be to minimise material removal while simultaneously achieving the lowest possible surface texture.

The average texture (Sa), as depicted in Figure 9C, levels out as the discharge coefficients measured for the samples exceed a Cd of 0.7. Sa, being an average value, does not fully characterise the surface and cannot be directly related to variations of Cd. To characterise the variations of Cd in relation to surface features, the surfaces were categorised based on their roughness peaks and on the density of these peaks. Reduced peak height (Spk) and density of peaks (Spd) are plotted in Figure 12A and B, respectively, alongside the channel

cross-sectional area. The Spk represents the mean height of peaks which are present above the core roughness based on an areal material ratio curve (~10% of surface) [93]. This representation allowed for a clear correlation between the surface treatment of a sample and the associated measured Cd.

In samples whose associated Cd was less than 0.7, roughness is primarily caused by partially adhered powder, accounting for more than 70% of the surface texture. Directional measurements, such as profile (Pa) and roughness (Ra), were also examined but did not provide sufficient resolution in the surface
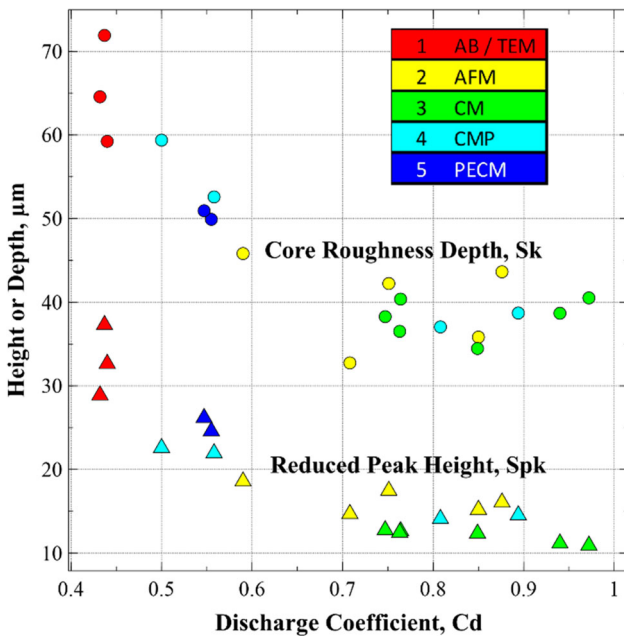


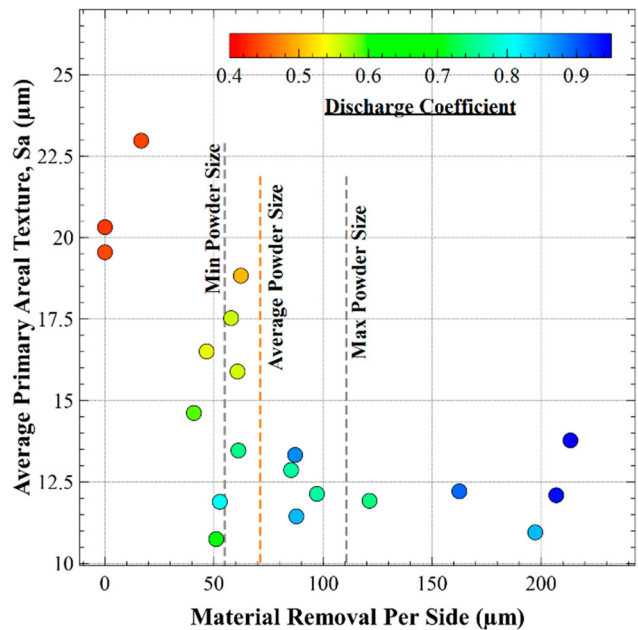**Figure 10.** Discharge coefficient in relation to core roughness and reduced peak height.



**Figure 11.** Average areal texture compared to material removal per side.
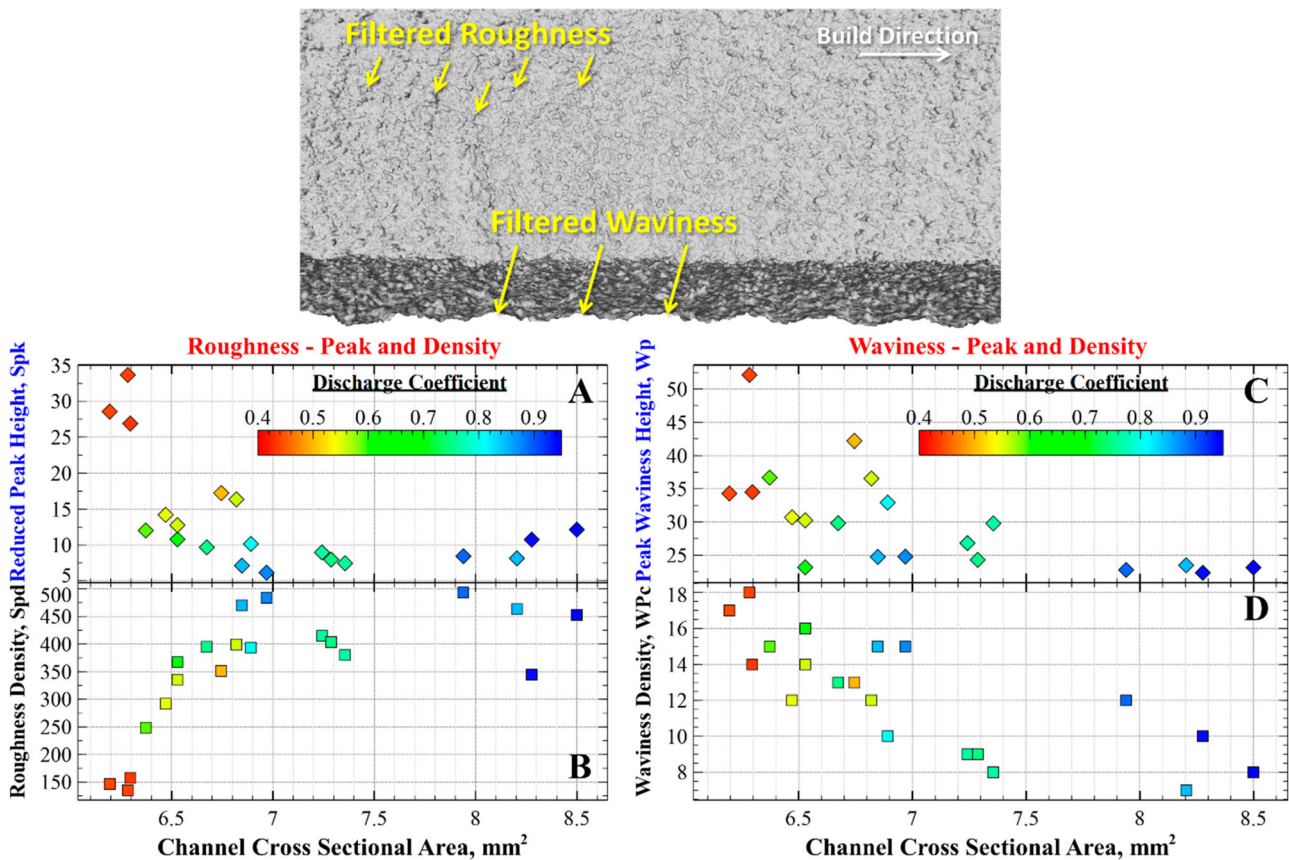
**Figure 12.** Channel cross sectional area compared to (A) Reduced peak height, Spk, (B) density of peaks, Spd, (C) waviness peak height, Wp, and (D) Density of waviness, WPc.

characterisation to correlate with measured Cd. This is an important result, since Ra is typically reported but is simply an average directional (single line) value. Since the peaks are one of the primary contributors to flow resistance, the Ra is insufficient to fully characterise the surface in case accurate Cd predictions are the final objective.

In addition to the peak height (Spk), the density of the peaks (Spd) also contributes to flow resistance, as illustrated in Figure 12B. Spd is traditionally used for bearing surface evaluation and would indicate a larger contact surface area. For surface enhancements and flow characterisation, higher Spd values imply that there are more peaks per unit area but that they have been smoothed away. The samples featuring the lowest Cd were planarised, thus they the peaks were smoothed and this is correlated with higher Spd values.

Waviness was also evaluated using a cutoff filter of 0.8 mm. Waviness is visually observed in all samples (Figure 8). However, samples whose internal surfaces are characterised by identical waviness value still generated flows with significantly different Cd. To better explain this phenomenon, the waviness peaks (Wp) were evaluated and their values suggest that lowered

peaks cause an increase of Cd, as seen in Figure 12C. The waviness valleys (Wv) were also evaluated and cannot be correlated to Cd. To further validate the result of the waviness peaks, the periodic waviness peak density (Wpc) was analysed and it was observed that it features different values for samples associated with higher Cd. Wpc is defined as the number of peaks per the unit length. In this case the sampling length was 38 mm. As the density of the waviness decreases, the Cd increases. The CM samples featured the lowest Wpc, which was approximately 50% lower than that of the as-built samples. It is observed that the waviness has a stronger impact on samples associated with Cd greater than 0.7.

These observations indicate that an effective surface enhancement process should remove the partially and fully adhered powder particles (roughness peaks and their density) and smooth the waviness peaks and density thereof to reduce resistance within the channel. It is important to note that, as the peak waviness decreases, the average waviness decreases, but then valleys eventually become the primary contributor to the flow resistance. Achieving full planarisation of a surface necessitates reducing both peaks and valleys

related to waviness, requiring a larger amount of material removal.

The impact of the combined texture effects is corroborated by the analysis results depicted in Figure 13, namely the comparison between a ratio of roughness peak/density (Spk/Spd) with waviness peak/density (Wp/WPc). Cd increases significantly with lower values of roughness and density. As the roughness ratio approaches 0.04, a trend can be observed: the surface waviness begins to exert a more pronounced influence on the increase of Cd. However, to reduce the waviness necessitates more material removal compared to the roughness and an increase in surface area for planarisation.

The experimental data underscored that an increase in area causes an increase of Cd, as expected. According to this experiment, approximately 65% of Cd variation can be attributed to changes in area. The wetted perimeter also contributes to flow resistance (8%). The ideal perimeter should match the mathematical definition, in theory, but in application varies along with the area. For instance, in a square channel, each sidewall is fully planarised or flat. The surface texture accounts for approximately 25% of the variation in Cd. The surface roughness due to the adhered powder and waviness resulting from irregular melt pools and build layering affect not only the perimeter, but also the overall 3D surface in the direction of the flow. This is evident since in several channels that had the same perimeter and channel area, the Cd varied based on the resulting texture due to the various surface enhancements.
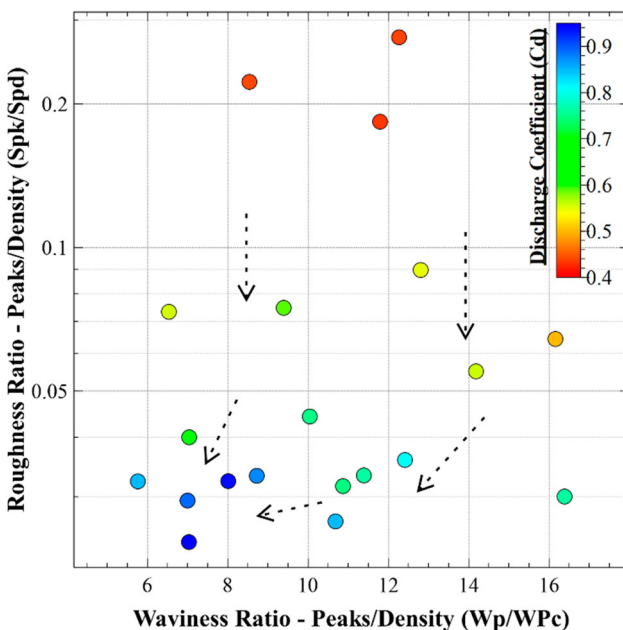


**Figure 13.** Ratio of roughness peaks to density (Spk/Spd) compared to the ratio of waviness peak to density (Wp/WPc).

The goal of this testing and characterisation was to demonstrate differences in surfaces resulting from each of the surface enhancement processes. The performance from each of the different microchannels with surface enhancements, along with a comparison to as-built baseline samples was summarised in Table 2. Chemical milling and CMP demonstrated the potential to reduce or eliminate the powder adherence and minimise waviness. However, these processes also removed the most material. Sample CM-17 featured some of the lowest peak and density values for roughness and waviness and with a slightly larger area would have likely achieved a performance in terms of Cd equal to that provided by the samples associated with the highest Cd. The evaluated surface enhancement technologies could also be improved by adopting optimised process parameters. One goal may be to minimise material removal while achieving a reduction of roughness and waviness peaks and density. The material removal must be balanced with the processing economics, as increased material removal increases the cost.

## 4. Conclusions

This work demonstrated that various surface enhancements can be applied to internal square microchannel samples produced using LP-DED with 1 mm thick walls. The samples featured a 2.54×2.54 mm square cross section and were built using the NASA HR-1 (Fe-Ni-Cr) alloy. Several techniques were demonstrated including abrasive flow machining (AFM), chemical milling (CM), chemical mechanical polishing (CMP), electrochemical machining (PECM), and thermal energy method (TEM) to modify the internal surfaces. Flow testing was performed to characterise the flow resistance of the resulting channel surfaces and the samples were then destructively evaluated using SEM, μ-CT, optical microscopy, and optical surface texture. The goal of this study was to demonstrate how variations in the LP-DED surfaces can be obtained, and to understand the underlying causes for corresponding changes in the resulting flow resistance. This data could then be used to provide requirements for additively manufactured components, such as heat exchanges.

The following conclusions can be drawn:

- The various surface enhancements result in different surface characteristics deriving from the mechanics of the process. These include: remnant powder, jagged edges and crystals, scratches, pitting or selective grain boundary attack.

- The CM and CMP processes removed the largest amount of material per side (up to 213 µm) resulting in a larger cross-sectional area (36%) compared to the as-built samples.
- The as-built perimeter was 32% longer than nominal perimeter (the design perimeter). This is due to the adhered powder particles and surface irregularities resulting from the melt pool and build layering.
- A 121% increase in Cd could be achieved using chemical milling with a 36% increase in area.
- 65% of the change in flow resistance is attributed to the area change; 8% depends on the perimeter and 25% on the surface texture.
- To increase the Cd, the surface enhancement process should eliminate adhered powder (roughness peaks and their density) and planarise peaks and density related to waviness. This implies that an effective surface enhancement process necessitates reducing both peaks and density thereof related to surface roughness and waviness, requiring increased material removal.
- The material removal should be at least equal to the average powder diameter (70 µm) to achieve reductions in flow resistance. While material removal equal to the minimum powder diameter (45 µm) results in 90% of powder elimination, it also result in significant variations of Cd.
- The ratio of roughness and waviness peak and density (Spk/Spd and Wp/WPc) is proposed as a relevant surface characterisation parameter. Using this parameter, it is possible to observe a transition where the effect of surface roughness due to peaks is reduced, and a reduction of the surface waviness is required to increase the Cd.

The application of surface enhancements to surface geometries obtained with the LP-DED process demonstrated that a surface could be modified based on a set of requirements. This data along with future testing can tailor a surface for fluid friction factors, fatigue life, corrosion, heat transfer, or even aesthetics. This is particularly important in heat exchangers, where each of these attributes are balanced during the design process. A combination of the LP-DED process and surface enhancements can be used to fabricate large scale components for aerospace, power generation, and industrial heat exchangers. Future research might combine processes, such as AFM and CM/CMP, using the advantages of the unique surfaces from each. This study engaged commercial vendors for the development of surface enhancements. It is anticipated that these processes could be effectively and economically utilised for future applications requiring surface variations to meet specific requirements.

## Disclosure statement

No potential conflict of interest was reported by the author(s).

## Data availability statement

The data presented in this study are available on request from the corresponding author.

## Author contributions

P.R.G. – Conceptualisation, Methodology, Writing – Original Draft, Data curation, Formal analysis, Funding acquisition, Investigation, Resources; A.C. – Supervision, Review & Editing, Methodology; P.C. – Supervision, Review & Editing, Methodology.

## ORCID

*Paul Gradl* http://orcid.org/0000-0002-2861-3410
*Angelo Cervone* http://orcid.org/0000-0001-5231-7948
*Piero Colonna* http://orcid.org/0000-0001-6446-8823

## References

[1] Gradl P, Tinker D, Park A, et al. Robust metal additive manufacturing process selection and development for aerospace components. J Mater Eng Performance, 2021;31:6013–6044. doi:10.1007/s11665-022-06850-0
[2] Blakey-Milner B, Gradl P, Snedden G, et al. Metal additive manufacturing in aerospace: a review. Mater Des. 2021;209:110008. doi:10.1016/j.matdes.2021.110008
[3] Yadroitsev I, Yadroitsava I, Du Plessis A, et al. *Fundamentals of laser powder bed fusion of metals*. 1st ed. Amsterdam: Elsevier; 2021. Available from: https://www.elsevier.com/books/fundamentals-of-laser-

powder-bed-fusion-of-metals/yadroitsev/978-0-12-824090-8 (accessed September 24, 2021)

[4] Niknam SA, Mortazavi M, Li D. Additively manufactured heat exchangers: a review on opportunities and challenges. Int J Adv Manuf Technol. 2021;112:601–618. doi:10.1007/s00170-020-06372-w

[5] Gradl P, Cervone A, Colonna P. Integral channel nozzles and heat exchangers using additive manufacturing directed energy deposition NASA HR-1 Alloy, in: 73rd International Astronautical Congress, Paris, France, 2022: p. IAC-22,C4,2,x73690.

[6] Kaur I, Singh P. State-of-the-art in heat exchanger additive manufacturing. Int J. Heat Mass Transf. 2021;178:121600. doi:10.1016/j.ijheatmasstransfer.2021.121600

[7] McDonough JR. A perspective on the current and future roles of additive manufacturing in process engineering, with an emphasis on heat transfer. Therm Sci Eng Prog. 2020;19:100594. doi:10.1016/j.tsep.2020.100594

[8] Favero G, Bonesso M, Rebesan P, et al. Additive manufacturing for thermal management applications: from experimental results to numerical modeling. Int J Thermofluids. 2021;10:100091. doi:10.1016/j.ijft.2021.100091

[9] da Silva RPP, Mortean MVV, de Paiva KV, et al. Thermal and hydrodynamic analysis of a compact heat exchanger produced by additive manufacturing. Appl Therm Eng. 2021;193:116973. doi:10.1016/j.applthermaleng.2021.116973

[10] Arman S, Lazoglu I. A comprehensive review of injection mold cooling by using conformal cooling channels and thermally enhanced molds. Springer London; 2023. doi:10.1007/s00170-023-11593-w

[11] Martina F, Mehrpouya M, Gisario A, et al. Metal additive manufacturing in the commercial aviation industry: a review. J Manuf Syst. 2019;53:124–149. doi:10.1016/j.jmsy.2019.08.005

[12] Ngo TD, Kashani A, Imbalzano G, et al. Additive manufacturing (3D printing): a review of materials, methods, applications and challenges. Compos Part B Eng. 2018;143:172–196. doi:10.1016/j.compositesb.2018.02.012

[13] Marshall G, Thompson S, Daniewicz S, et al. Estimating the effects of part size on direct laser deposition parameter selection via a thermal resistance network approach, solid free. Fabr. 2016 Proc. 27th Annu. Int. Solid Free. Fabr. Symp. – An Addit. Manuf. Conf. (2016) 350–364. http://utw10945.utweb.utexas.edu/sites/default/files/2016/024-Marshall.pdf.

[14] Berez J, Praniewicz M, Saldana C. Assessing laser powder bed fusion system geometric errors through artifact-based methods. Procedia Manuf. 2021;53:395–406. doi:10.1016/j.promfg.2021.06.042

[15] Fotovvati B, Asadi E. Size effects on geometrical accuracy for additive manufacturing of Ti-6Al-4 V ELI parts. Int J Adv Manuf Technol. 2019;104:2951–2959. doi:10.1007/s00170-019-04184-1

[16] Gradl PR, Tinker DC, Ivester J, et al. Geometric feature reproducibility for Laser Powder Bed Fusion (L-PBF) additive manufacturing with Inconel 718. Addit Manuf. 2021;47:102305. doi:10.1016/j.addma.2021.102305

[17] Çalışkan CI, Özer G, Coşkun M, et al. Investigation of direct metal laser sintering downskin parameters ' sagging effect on microchannels. Int J Adv Manuf Technol. 2021;114:2567–2575. doi:10.1007/s00170-021-07057-8

[18] Snyder JC, Thole KA. Effect of additive manufacturing process parameters on turbine cooling. J. Turbomach. 2020;142:051007. doi:10.1115/1.4046459

[19] Careri F, Khan RHU, Todd C, et al. Additive manufacturing of heat exchangers in aerospace applications : A. Appl Therm Eng. 2023;235:121387. doi:10.1016/j.applthermaleng.2023.121387

[20] Kirsch KL, Thole KA. Heat transfer and pressure loss measurements in additively manufactured wavy microchannels. J Turbomach. 2016;139:011007: 16-1155. doi:10.1115/1.4034342

[21] Ferster KK, Kirsch KL, Thole KA. Effects of geometry, spacing, and number of pin fins in additively manufactured microchannel pin fin arrays. J Turbomach. 2017;140:011007: 17-1138. doi:10.1115/1.4038179

[22] Alsulami M, Mortazavi M, Niknam SA, et al. Design complexity and performance analysis in additively manufactured heat exchangers. Int J Adv Manuf Technol. 2020;110:865–873. doi:10.1007/s00170-020-05898-3

[23] Klein E, Ling J, Aute V, et al. A review of recent advances in additively manufactured heat exchangers. Int Refrig Air Cond Conf. 2018;2478:1–10. https://docs.lib.purdue.edu/iracc%0Ahttps://docs.lib.purdue.edu/iracc/1983.

[24] Kaur I, Singh P. Critical evaluation of additively manufactured metal lattices for viability in advanced heat exchangers. Int J Heat Mass Transf. 2021;168:120858. doi:10.1016/j.ijheatmasstransfer.2020.120858

[25] Zhang C, Wang S, Li J, et al. Additive manufacturing of products with functional fluid channels: a review. Addit Manuf. 2020;36:101490. doi:10.1016/j.addma.2020.101490

[26] Vafadar A, Guzzomi F, Hayward K. Experimental investigation and comparison of the thermal performance of additively and conventionally manufactured heat exchangers. Metals (Basel). 2021;11:574. doi:10.3390/met11040574

[27] Kerstens F, Cervone A, Gradl P. End to end process evaluation for additively manufactured liquid rocket engine thrust chambers. Acta Astronaut. 2021;182:454–465. doi:10.1016/j.actaastro.2021.02.034

[28] Gradl P, Mireles OR, Katsarelis C, et al. Advancement of extreme environment additively manufactured alloys for next generation space propulsion applications. Acta Astronaut. 2023;211:483–497. doi:10.1016/j.actaastro.2023.06.035

[29] Li SH, Kumar P, Chandra S, et al. Directed energy deposition of metals: processing, microstructures, and mechanical properties. Int Mater Rev. 2022;67:605–647. doi:10.1080/09506608.2022.2097411

[30] Svetlizky D, Das M, Zheng B, et al. Directed energy deposition (DED) additive manufacturing: physical characteristics, defects, challenges and applications. Mater Today. 2021;49:271–295. doi:10.1016/J.MATTOD.2021.03.020

[31] Gradl PR, Teasley TW, Protz CS, et al. Process development and hot-fire testing of additively manufactured NASA HR-1 for Liquid Rocket Engine Applications, in: AIAA Propuls. Energy. 2021;2021:1–23. doi:10.2514/6.2021-3236

[32] Shamsaei N, Yadollahi A, Bian L, et al. An overview of Direct Laser Deposition for additive manufacturing; Part II: mechanical behavior, process parameter optimization and control. Addit Manuf. 2015;8:12–35. doi:10.1016/j.addma.2015.07.002

[33] Soltani-tehrani A, Chen P, Katsarelis C, et al. Thin-walled structures mechanical properties of laser powder directed energy deposited NASA HR-1 superalloy: effects of powder reuse and part orientation. Thin-Walled Struct. 2023;185:110636. doi:10.1016/j.tws.2023.110636

[34] Melia MA, Duran JG, Koepke JR, et al. How build angle and post-processing impact roughness and corrosion of additively manufactured 316L stainless steel. Npj Mater Degrad. 2020;4:1–11. doi:10.1038/s41529-020-00126-5

[35] Boban J, Ahmed A. Improving the surface integrity and mechanical properties of additive manufactured stainless steel components by wire electrical discharge polishing. J Mater Process Technol. 2021;291:117013. doi:10.1016/j.jmatprotec.2020.117013

[36] Ye C, Zhang C, Zhao J, et al. Effects of post-processing on the surface finish, porosity, residual stresses, and fatigue performance of additive manufactured metals: a review. J Mater Eng Perform. 2021;30:6407–6425. doi:10.1007/s11665-021-06021-7

[37] [37] H. Fayazfar, J. Sharifi, M.K. Keshavarz, M. Ansari, *An overview of surface roughness enhancement of additively manufactured metal parts: a path towards removing the post-print bottleneck for complex geometries*, Springer London, 2023. doi:10.1007/s00170-023-10814-6

[38] Kumbhar NN, Mulay AV. Post processing methods used to improve surface finish of products which are manufactured by additive manufacturing technologies: a review. J Inst Eng Ser C. 2016;99:481–487. doi:10.1007/s40032-016-0340-z

[39] Hashmi AW, Mali HS, Meena A, et al. A comprehensive review on surface post-treatments for freeform surfaces of bio-implants. J Mater Res Technol. 2023;23:4866–4908. doi:10.1016/j.jmrt.2023.02.007

[40] Boban J, Ahmed A, Jithinraj EK, et al. *Polishing of additive manufactured metallic components: retrospect on existing methods and future prospects*. Springer London; 2022. doi:10.1007/s00170-022-09382-y

[41] Hashmi AW, Mali HS, Meena A, et al. Surface characteristics improvement methods for metal additively manufactured parts: a review. Adv Mater Process Technol. 2022;00:1–40. doi:10.1080/2374068X.2022.2077535

[42] Maleki E, Bagherifard S, Bandini M, et al. Surface post-treatments for metal additive manufacturing: progress, challenges, and opportunities. Addit Manuf. 2021;37:101619. doi:10.1016/j.addma.2020.101619

[43] Lee JY, Nagalingam AP, Yeo SH. A review on the state-of-the-art of surface finishing processes and related ISO/ASTM standards for metal additive manufactured components. Virtual Phys Prototyp. 2020;0:1–29. doi:10.1080/17452759.2020.1830346

[44] Manco E, Cozzolino E, Astarita A. Laser polishing of additively manufactured metal parts: a review. Surf Eng. 2022;38:217–233. doi:10.1080/02670844.2022.2072080

[45] De Oliveira D, Gomes MC, Dos Santos AG, et al. Abrasive and non-conventional post-processing techniques to improve surface finish of additively manufactured metals: a review. Prog Addit Manuf. 2023;8:223–240. doi:10.1007/s40964-022-00325-3

[46] Paul RG, Mireles OR, Protz CS, et al. *Metal additive manufacturing for propulsion applications*. 1st ed. Reston (VA): American Institute of Aeronautics and Astronautics, Inc.; 2022. doi:10.2514/4.106279

[47] Zhang J, Lee YJ, Wang H. A Brief review on the enhancement of surface finish for metal additive manufacturing. J Miner Met Mater Eng. 2021;7:1–14.

[48] Syrlybayev D, Seisekulova A, Talamona D, et al. The post-processing of additive manufactured polymeric and metallic parts. J Manuf Mater Process. 2022;6; doi:10.3390/jmmp6050116

[49] Yazdanparast S, Raikar S, Heilig M, et al. Iodine-based sensitization of copper alloys to enable self-terminating etching for support removal and surface improvements of additively manufactured components, 3D Print. Addit Manuf. 2023;10:619–630. doi:10.1089/3dp.2021.0242

[50] Nagalingam AP, Yeo SH. Surface finishing of additively manufactured Inconel 625 complex internal channels: a case study using a multi-jet hydrodynamic approach. Addit Manuf. 2020;36:101428. doi:10.1016/j.addma.2020.101428

[51] Nagalingam AP, Toh BL, Yeo SH. Surface polishing of laser powder bed fused Inconel 625 surfaces using multi-jet hydrodynamic cavitation abrasive finishing: an emerging class of cleaner surface enhancement process. Int J Precis Eng Manuf - Green Technol. 2023;10:637–657. doi:10.1007/s40684-022-00471-7

[52] Lesyk D, Dzhemelinskyi V, Mordyuk B, et al. Surface polishing of laser powder bed fused superalloy components by magnetic post-treatment. Proc. 2020 IEEE 10th Int. Conf. "Nanomaterials Appl. Prop. N; 2020(2020):10–13. doi:10.1109/NAP51477.2020.9309600

[53] Guo J, Au KH, Liu K, et al. A novel vibration-assisted magnetic abrasive polishing method for complex internal surface finishing. Proc. 17th Int. Conf. Eur. Soc. Precis. Eng. Nanotechnology, EUSPEN 2017. 2017: 161–162.

[54] Basha MM, Basha SM, Jain VK, et al. State of the art on chemical and electrochemical based finishing processes for additive manufactured features. Addit Manuf. 2022;58:103028. doi:10.1016/j.addma.2022.103028

[55] Favero G, Berti G, Bonesso M, et al. Experimental and numerical analyses of fluid flow inside additively manufactured and smoothed cooling channels. Int Commun Heat Mass Transf. 2022;135:106128. doi:10.1016/j.icheatmasstransfer.2022.106128

[56] Tyagi P, Goulet T, Riso C, et al. Reducing surface roughness by chemical polishing of additively manufactured 3D printed 316 stainless steel components. Int J Adv Manuf Technol. 2018;100:2895–2900. doi:10.1007/s00170-018-2890-0

[57] Mohammadian N, Turenne S, Brailovski V. Surface finish control of additively-manufactured Inconel 625 components using combined chemical-abrasive flow polishing. J Mater Process Technol. 2018;252:728–738. doi:10.1016/j.jmatprotec.2017.10.020

[58] Zhu Y, Zhou L, Wang S, et al. On friction factor of fluid channels fabricated using selective laser melting. Virtual Phys Prototyp. 2020;15:496–509. doi:10.1080/17452759.2020.1823093

[59] Zhou L, Zhu Y, Liu H, et al. A comprehensive model to predict friction factors of fluid channels fabricated using laser powder bed fusion additive manufacturing. Addit Manuf. 2021;47:102212. doi:10.1016/j.addma.2021.102212

[60] Çalışkan Cİ, Coşkun M, Özer G, et al. Investigation of manufacturability and efficiency of micro channels with different geometries produced by direct metal laser sintering. Int J Adv Manuf Technol. 2021;117:3805–3817. doi:10.1007/s00170-021-07928-0

[61] B.K.J. Evangelista, Laser powder bed fusion-induced surface roughness and effects on thermal fluid performance for additively manufactured metals in liquid rocket components, California State University, 2022.

[62] Seltzman AH, Wukitch SJ. Surface roughness and finishing techniques in selective laser melted GRCop-84 copper for an additive manufactured lower hybrid current drive launcher. Fusion Eng. Des. 2020;160:111801. doi:10.1016/j.fusengdes.2020.111801

[63] W. Demisse, J. Xu, L. Rice, P. Tyagi, Review of internal and external surface finishing technologies for additively manufactured metallic alloys components and new frontiers, Prog Addit Manuf. 2023;8:1433–1453. doi:10.1007/s40964-023-00412-z

[64] Min Z, Wu Y, Yang K, et al. Dimensional characterizations using scanning electron microscope and surface improvement with electrochemical polishing of additively manufactured microchannels. J Eng Gas Turbines Power. 2021;143:1–12. doi:10.1115/1.4049908

[65] Jiang D, Tian Y, Zhu Y, et al. Investigation of surface roughness post-processing of additively manufactured nickel-based superalloy Hastelloy X using electropolishing. Surf Coatings Technol. 2022;441:128529. doi:10.1016/j.surfcoat.2022.128529

[66] An L, Wang D, Zhu D. Combined electrochemical and mechanical polishing of interior channels in parts made by additive manufacturing. Addit Manuf. 2022;51:102638. doi:10.1016/j.addma.2022.102638

[67] Chaghazardi Z, Wüthrich R. Review—electropolishing of additive manufactured metal parts. J Electrochem Soc. 2022;169:043510. doi:10.1149/1945-7111/ac6450

[68] Ferchow J, Baumgartner H, Klahn C, et al. Model of surface roughness and material removal using abrasive flow machining of selective laser melted channels. Rapid Prototyp J. 2020;26:1165–1176. doi:10.1108/RPJ-09-2019-0241

[69] M. Buchholz, S. Gruber, A. Selbmann, A. Marquardt, L. Meier, M. Müller, L. Seifert, C. Leyens, M. Tajmar, C. Bach, Flow rate improvements in additively manufactured flow channels suitable for rocket engine application. CEAS Sp J. 2022;15:715–728. doi:10.1007/s12567-022-00476-7

[70] Han S, Salvatore F, Rech J, et al. Abrasive flow machining (AFM) finishing of conformal cooling channels created by selective laser melting (SLM). Precis Eng. 2020;64:20–33. doi:10.1016/j.precisioneng.2020.03.006

[71] Duval-Chaneac MS, Han S, Claudin C, et al. Experimental study on finishing of internal laser melting (SLM) surface with abrasive flow machining (AFM). Precis Eng. 2018;54:1–6. doi:10.1016/j.precisioneng.2018.03.006

[72] Soltani-tehrani A, Chen P, Katsarelis C, et al. Laser powder directed energy deposition (LP-DED) NASA HR-1 alloy: laser power and heat treatment effects on microstructure and mechanical properties. Addit Manuf Lett. 2022;3:100097. doi:10.1016/j.addlet.2022.100097

[73] Gradl P, Cervone A, Colonna P. Influence of build angles on thin-wall geometry and surface texture in laser powder directed energy deposition. Mater Des. 2023;234:112352. doi:10.1016/j.matdes.2023.112352

[74] Gradl PR, Cervone A, Gill E. Surface texture characterization for thin-wall NASA HR-1 Fe – Ni – Cr alloy using laser powder directed energy deposition (LP-DED). Adv. Ind. Manuf. Eng. 2022;4:100084. doi:10.1016/j.aime.2022.100084

[75] Chen PS, Katsarelis CC, Medders WM, et al. Development of directed energy deposited NASA HR-1 to optimize properties for Liquid Rocket Engine Applications, NASA Tech. Memo. NASA/TM–20; 2023.

[76] Obilanade D, Dordlofva C, Törlind P. Surface roughness considerations in design for additive manufacturing - a literature review. Proc Des Soc. 2021;1:2841–2850. doi:10.1017/pds.2021.545

[77] Wahab Hashmi A, Singh Mali H, Meena A. Improving the surface characteristics of additively manufactured parts: a review. Mater Today Proc. 2021;81:723–738. doi:10.1016/j.matpr.2021.04.223

[78] M. Rauch, J. Hascoet, Improving additive manufactured surfaces properties with post processing techniques. 2021.

[79] Tan KL, Yeo S-HH, Ong CH. Nontraditional finishing processes for internal surfaces and passages: a review. Proc Inst Mech Eng Part B J Eng Manuf. 2016;231:2302–2316. doi:10.1177/0954405415626087

[80] Yadav SK, Singh MK, Singh BR. Effect of unconventional machining on surface roughness of metal: aluminum and brass- a case study of abrasive flow. SAMRIDDHI A J Phys Sci Eng Technol. 2015;2:53–60. doi:10.18090/samriddhi.v2i1.1598

[81] Diaz A. Surface texture characterization and optimization of metal additive manufacturing-produced components for aerospace applications. Addi Manuf Aerosp Ind. 2019;16:341–374. doi:10.1016/B978-0-12-814062-8.00018-2

[82] Tyagi P, Goulet T, Riso C, et al. Reducing the roughness of internal surface of an additive manufacturing produced 316 steel component by chempolishing and electropolishing. Addit Manuf. 2019;25:32–38. doi:10.1016/j.addma.2018.11.001

[83] Kulkarni M, Gao F, Liang H. Chemical-mechanical polishing (CMP): a controlled tribocorrosion process. Tribocorrosion Passiv Met Coatings. 2011;18:498–518e. doi:10.1533/9780857093738.3.498

[84] Kim US, Park JW. High-quality surface finishing of industrial three-dimensional metal additive manufacturing using electrochemical polishing. Int J Precis Eng Manuf - Green Technol. 2019;6:11–21. doi:10.1007/s40684-019-00019-2

[85] Sergiy P, Popov V, Shypul O, et al. Advanced thermal energy method for finishing precision parts. In: K Gupta, A Pramanik, editor. *Advanced Machining Finished*. Amsterdam: Elsevier; 2021. p. 527–575. doi:10.1016/C2018-0-00908-1

[86] Fritz A, Sekol L, Koroskenyi J, et al. Experimental analysis of thermal energy deburring process by design of experiment, in: American Society of Mechanical Engineers (ASME) (Ed.), ASME 2012 Int. Mech. Eng. Congr. Expo.,

Houston, TX USA, 2012: pp. 2035–2041. doi:10.1115/IMECE2012-88411

[87] Schneider CA, Rasband WS, Eliceiri KW. NIH Image to ImageJ: 25 years of image analysis. Nat Methods. 2012;9:671–675. doi:10.1038/nmeth.2089

[88] Marinello F, Pezzuolo A. Application of ISO 25178 standard for multiscale 3D parametric assessment of surface topographies. IOP Conf Ser Earth Environ Sci. 2019;275:012011. doi:10.1088/1755-1315/275/1/012011

[89] International Organization for Standardization. ISO 25178-2 Geometrical product specifications (GPS) — surface texture: Areal — Part 2: Terms, definitions and surface texture parameters, Geneva, 2021. https://www.iso.org/standard/74591.html.

[90] du Plessis A, Yadroitsev I, Yadroitsava I, et al. Le Roux, X-Ray microcomputed tomography in additive manufacturing: a review of the current technology and applications, 3D print. Addit Manuf. 2018;5:227–247. doi:10.1089/3DP.2018.0060

[91] Wang X, Li S, Fu Y, et al. Finishing of additively manufactured metal parts by abrasive flow machining, Solid Free. Fabr. 2016 Proc. 27th Annu. Int. Solid Free. Fabr. Symp. - An Addit. Manuf. Conf. SFF; 2016. (2016) 2470–2472.

[92] Maurer O, Herter F, Bähre D. The impact of manufacturing parameters on corrosion resistance of additively manufactured AlSi10Mg-samples: a design of experiments approach. Manuf. Lett. 2022;34:29–33. doi:10.1016/j.mfglet.2022.08.006

[93] Franco LA, Sinatora A. 3D surface parameters (ISO 25178-2): Actual meaning of Spk and its relationship to Vmp. Precis. Eng. 2015;40:106–111. doi:10.1016/j.precisioneng.2014.10.011